The Astrophysical Journal Supplement Series, 168:19–57, 2007 January

THE HOST GALAXIES AND ENVIRONMENT OF *CHANDRA*-SELECTED ACTIVE GALACTIC NUCLEI IN THE DEEP ACS GTO CLUSTER FIELDS[1]

André R. Martel,[2] Felipe Menanteau,[2,3] Paolo Tozzi,[4] Holland C. Ford,[2] and Leopoldo Infante[5]

Received 2006 April 11; accepted 2006 September 2

ABSTRACT

We present catalogs and images of optical counterparts to the *Chandra*-selected X-ray sources found in the fields of the five clusters RX J0152−1357, RX J0849+4452, RDCS J0910+5422, MS 1054−0321, and RDCS J1252−2927, which were imaged with the Advanced Camera for Surveys as part of the ACS Guaranteed Time Observer programs. A total of 98 X-ray sources fall within the ACS mosaics, and positive identifications are made for ∼96% of them, including confirmed cluster members. We classify the sources as active galactic nuclei (AGNs) or QSOs depending on their X-ray output. The $\log N(>S)-\log S$ test indicates a significant overdensity of X-ray sources in the RX J0152−1357, RDCS J0910+5422, and MS 1054−0321 fields with respect to the CDF-S, suggesting an association of some X-ray sources with the large-scale structure of the clusters. From the asymmetry and concentration indices, ∼52% of the optical counterparts are early-type galaxies, ∼35% late-type, and the remainder irregular. A blue core is found in approximately half of the early-type galaxies. From visual examination, approximately 40% of the counterparts possess an unresolved nucleus, a common signature of nuclear activity. A majority of these nuclei are found in near face-on late-type galaxies although selection effects might be important. The X-ray to optical flux ratio of the nuclei correlates with the inclination angle of the late-type galaxies but not of the early types, as expected if dust is significant in the circumnuclear regions. The AGNs possess a ∼50% excess of nearby companions compared to the overall galaxy population in the same fields. The surface density of the X-ray sources is highest at projected radii of $\lesssim$1 Mpc from the cluster center and relatively flat at larger radii. We describe the morphology and environment of the cluster members and compare them with the other optical counterparts.

Subject headings: galaxies: active — galaxies: clusters: general — galaxies: clusters: individual (RX J0152−1357, RX J0849+4452, RDCS J0910+5422, MS 1054−0321, RDCS J1252−2927) — X-rays: galaxies: clusters

Online material: color figures

1. INTRODUCTION

The prevalence of active galactic nuclei (AGNs) in clusters, as well as the evolution of the AGN fraction with cosmic time, is still a matter of contention. Results from optical spectroscopic surveys of moderate redshift clusters (e.g., Dressler et al. 1999) indicated that the fraction of AGNs in the clusters is roughly consistent with the field population (∼1%–2%). But *ROSAT* and *Chandra* X-ray observations revealed an excess of luminous X-ray point sources in the direction of low-z Abell clusters as well as moderate redshift clusters (e.g., Cappi et al. 2001: 3C 295, $z = 0.46$ and RX J003033+261819, $z = 0.5$; Molnar et al. 2002: Abell 1995, $z = 0.32$ and MS 0451.6−0304, $z = 0.55$; Sun & Murray 2002: Abell 1367, $z = 0.022$). Follow-up spectroscopic campaigns confirmed that several of these X-ray sources are in fact associated with cluster members, thus significantly increasing the AGN content in clusters to several percent e.g., ∼5% in Abell 2104 (Martini et al. 2002) and ∼12% in Abell 1367. Tantalizing evidence of enhanced AGN activity and spatially correlated X-ray–selected AGNs is also found in large-scale structures not necessarily associated with clusters (Gilli et al. 2003).

The mechanisms responsible for triggering nuclear activity in high-z clusters, and any connection with star formation activity, also remain to be explored rigorously. Do cluster AGNs follow similar evolutionary trends as blue star-forming spiral galaxies in clusters? Are the AGNs found in high-density environments? Homeier et al. (2005) find no star-forming galaxies at radii $R \lesssim$ 500 kpc from the center of the ACS GTO clusters, where the galaxy density is highest. They attribute this distribution to ram-pressure stripping of the cold gas by the intracluster medium. On the other hand, more mergers and interactions are found in high-z clusters (e.g., van Dokkum et al. 1999,2000, for MS 1054−0321) than in local clusters. Also, AGNs in low-z clusters do not necessarily exhibit the classical spectroscopic signatures of field AGNs, such as strong emission lines, suggesting highly unusual conditions in the narrow-line region and possibly in the gas reservoir that fuels the central black hole (and the star-forming regions; Martini et al. 2002).

The host galaxies of AGNs at $z \approx 1$, whether in the field or in clusters, have hardly been investigated. Do active nuclei reside in a preferred type? In low-z clusters, the AGN hosts appear to consist of a mix of old, red ellipticals and blue spirals, implying that the nuclear activity is episodic (Martini et al. 2002). From the GEMS field survey, Sánchez et al. (2004) find that 80% of AGN hosts at $0.5 < z < 1.1$ are bulge-dominated, while the rest are disk-dominated. There is also some evidence that AGN spheroids possess bluer colors than normal spheroids. Also, Grogin et al. (2003, 2005) report no differences in the asymmetries

[1] Based on observations made with the NASA / ESA *Hubble Space Telescope*, which is operated by AURA, Inc., under NASA contract NAS 5-26555.

[2] Department of Physics and Astronomy, Johns Hopkins University, Baltimore, MD; martel@pha.jhu.edu, felipe@pha.jhu.edu, tozzi@ts.astro.it, ford@pha.jhu.edu.

[3] Current address: Department of Physics and Astronomy, Rutgers University, Piscataway, NJ.

[4] INAF—Osservatorio Astronomico di Trieste, Italy.

[5] Departmento de Astronomía y Astrofísica, Pontificia Universidad Católica de Chile, Santiago, Chile; linfante@astro.puc.cl.

TABLE 1
Journal of the ACS Observations

Cluster (1)	z_{cl} (2)	R.A. (J2000.0)[a] (3)	Decl. (J2000.0)[a] (4)	Mosaic Dimensions (arcmin) (5)	Filters[b] (6)
RX J0152−1357	0.837	01 52 44	−13 57 15	5.9 × 6.1	r_{625}(26.8), i_{775}(26.6), z_{850}(26.0)
RX J0849+4452 (Lynx)	1.266	08 48 46	44 53 00	3.4 × 9.8	i_{775}(26.8), z_{850}(26.4)
RDCS J0910+5422	1.101	09 10 45	54 22 15	3.4 × 3.7	i_{775}(26.7), z_{850}(26.4)
MS 1054−0321	0.831	10 56 59	−03 37 15	6.0 × 6.0	V_{606}(26.6), i_{775}(26.4), z_{850}(25.8)
RDCS J1252−2927	1.235	12 52 54	−29 27 10	5.7 × 5.8	i_{775}(26.7), z_{850}(26.4)

[a] The positions of the center of the mosaic are listed. Units of right ascension are hours, minutes, and seconds, and units of declination are degrees, arcminutes, and arcseconds.
[b] The limiting magnitude in a 1″ wide circular aperture is listed in parenthesis after the filter name for a 5 σ detection.

between active and normal host galaxies at $0.4 < z < 1.3$ in GOODS. What is the distribution of the AGN morphological types in high-z clusters, how is it related to the local density, and how does it compare to field AGNs?

As part of the Guaranteed Time Observer (GTO) program of the Advanced Camera for Surveys (ACS; Ford et al. 2003) Science Team, deep multicolor imaging of several X-ray–selected clusters at $z \approx 1$ was performed to address important problems regarding their morphology-density relation (Postman et al. 2005), their evolutionary mechanisms and luminosity functions (Goto et al. 2005; Holden et al. 2005), their color-magnitude relations (Blakeslee et al. 2003b; Mei et al. 2006), and their star-forming properties (Homeier et al. 2005). We have begun examining in detail the AGN population of the clusters. The AGNs are identified from deep *Chandra* X-ray images and so their identifications are less influenced by absorption than in the optical bands. The superior angular resolution of the *Hubble Space Telescope* (*HST*) ACS and the great depth of the images allow for the first time a comprehensive study of the structural parameters of their host galaxies, their morphological types, their resolved colors, and their environment when the universe was half its current age. The ACS imaging greatly augments previous *HST* Wide Field Planetary Camera 2 (WFPC2) observations of some of these clusters.

Our goal is to determine the AGN fraction and distribution in the environment of the $z \approx 1$ ACS GTO clusters and to compare them to a field population to ultimately characterize their formation and fueling scenarios. As a first step toward this goal, we present the optical candidates to the *Chandra* sources in the ACS GTO cluster fields. We determine the X-ray excess in the cluster fields with the $\log N(>S)$–$\log S$ method, we identify the optical candidates, we present their images, and we tabulate their global properties. Unfortunately, only a few reliable spectroscopic and photometric redshifts are currently available, and so cluster membership can be conclusively ascertained for only a few sources.

2. OBSERVATIONS AND PROCESSING

2.1. *The ACS Observations*

All five clusters of the sample were observed as part of the ACS GTO programs 9290 and 9919 in Cycles 11 and 12. The observing strategy, the choice of filters, and the processing of the images are discussed in detail in Postman et al. (2005). A journal of the observations is tabulated in Table 1. The Lynx field includes the two clusters RX J0849+4452 ($z = 1.261$) and RX J0849+4453 ($z = 1.273$) (Rosati et al. 1999; Stern et al. 2002). All the clusters were imaged with the Wide Field Channel (WFC) of ACS through two or three of the F606W (V_{606}), F625W (r_{625}), F775W (i_{775}), and F850LP (z_{850}) filters in multiple pointings that were assembled into mosaics with the ACS Science Analysis Pipeline (APSIS; Blakeslee et al. 2003a). Total integration times in each filter varied from 2000 to 12,000 s which correspond to a range of 1–5 orbits per pointing. Limiting magnitudes calculated with the RMS maps generated by APSIS in 1″ wide circular apertures away from the cluster center for a 5 σ detection are listed in col. (6) of Table 1. Each mosaic was drizzled to a final spatial scale of 0.05″ pixel^{-1}. All the magnitudes are expressed in the AB system and are corrected for Galactic extinction using the maps of Schlegel et al. (1998). To simplify the notation, we will refer to RX J0152−1357 as RX J0152, RX J0849+4452 as RX J0849, RDCS J0910+5422 as RDCS J0910, MS 1054−0321 as MS 1054, and RDCS J1252−2927 as RDCS J1252 in the remainder of this work.

Detection, photometry, and photometric redshift catalogs were automatically generated with SExtractor (Bertin & Arnouts 1996) and BPZ (Bayesian Photometric Redshifts; Benítez 2000). A so-called "detection image" was created for each cluster by combining all of its images weighed by their respective inverse variance. Visual classification into common Hubble morphological types were made by Postman et al. for all the galaxies with $i_{775} < 23.5$ for RX J0152 and MS 1054 and $z_{850} < 24$ for RX J0849, RDCS J0910, and RDCS J1252. We use their classifications but revise some based on our own careful examination. At fainter magnitudes, the visual classifications are unreliable. For consistency with the automatic classification presented below (§ 3.2), we bin the Postman et al. subcategories into three coarser groups: early-type (ellipticals and S0s), late-type (spirals), and irregulars/peculiars.

The redshifts were taken from the tabulation of Postman et al. (2005) and references therein. These consist of ground-based spectroscopic redshifts, primarily for the brighter sources, as well as photometric redshifts. The photometric redshifts for RX J0152 and MS 1054 are derived from the three ACS bandpasses; only the most secure redshifts are considered (Bayesian ODDS $\geq$0.9). No reliable photometric redshifts can be evaluated from the two filters of RX J0849 and RDCS J0910. The photometric redshifts of RDCS J1252 are based on the two ACS filter bandpasses augmented with *BVJK* ground photometry. As an additional verification of the spectroscopic redshifts, the optical candidates were cross-correlated with the NASA Extragalactic Database.

2.2. *The Chandra Observations*

A journal of the *Chandra* observations of the five clusters in our study is presented in Table 2. These data have been presented

TABLE 2
JOURNAL OF THE *Chandra* OBSERVATIONS

Cluster (1)	Observation ID (PI) (2)	Observation Date (3)	Exposure Time[a] (ks) (4)	References (5)
RX J0152−1357	913 (Ebeling)	2000 Sep 8	36	1
RX J0849+4452	927 (Stanford)	2000 May 4	186	2, 3
	1708 (Stanford)	2000 May 3		
RDCS J0910+5422	2227 (Stanford)	2001 Apr 29	170	4
	2452 (Stanford)	2001 Apr 24		
MS 1054−0321	512 (Garmire)	2000 Apr 21	80	5, 6
RDCS J1252−2927	4198 (Rosati)	2003 Mar 20	188	7
	4403 (Rosati)	2003 Mar 18		

[a] Total exposure time of the combined data sets.

REFERENCES.—(1) Maughan et al. 2003; (2) Stanford et al. 2001; (3) Stern et al. 2002; (4) Stanford et al. 2002; (5) Jeltema et al. 2001; (6) Johnson et al. 2003; (7) Rosati et al. 2004.

in previous work (see references in col. [4] of Table 2) but we have performed our own reduction and analysis with the latest calibration files, which we summarize in the following. The four clusters RX J0152, RX J0849, RDCS J0910, and RDCS J1252 were imaged on the ACIS-I array in VFAINT mode, while MS 1054 was observed with ACIS-S in FAINT mode. The images were restricted to the soft (0.5–2 keV) and hard (2–7 keV) energy bands. The size of their exposed regions is approximately $17' \times 17'$, easily encompassing the smaller field of view of the ACS images. The *Chandra* Lynx field covers the two ACS clusters at $z \approx 1.266$ as well as a third cluster, RX J0849+4456 ($z = 0.571$).

The X-ray images were reduced with well established techniques by one of us (P. Tozzi). The data were processed with the *Chandra* Interactive Analysis of Observations software package version 2.3 (CIAO 2.3) and calibrated with the *Chandra* Calibration Database version 2.26 (CALDB 2.26), except for RDCS J0910, which was treated with CALDB version 3.0.3. The data were filtered to include only the standard event grades 0, 2, 3, 4, and 6. All hot pixels and columns were rejected. Flickering pixels with more than two events contiguous in time, where a single time interval was set to 3.3 s, were removed. Time intervals with background rates larger than 3 σ over the quiescent value were also removed.

Source catalogs were generated from the combined X-ray images with SExtractor (Bertin & Arnouts 1996). The source extraction was performed on the soft, hard, and total band (0.5–7 keV) images rebinned by a factor of 2, so that one image pixel corresponds to $0.984''$. SExtractor detection parameters were chosen as a result of simulations (see Tozzi et al. 2001 for details). SExtractor is not tailored for use with a very low and sparse background as in ACIS-I, so we used a modified version of the program to allow an external map to be used as local background. This smoothed map was computed from the data themselves after removal of the sources down to a very low threshold. This modified detection algorithm has been adopted in the *Chandra* Deep Field–South (Rosati et al. 2002) and in the Lynx Field (Stern et al. 2002).

After combining all the sources found with SExtractor, we measured the aperture photometry and the signal-to-noise ratio of all the candidate detections in the area of extraction of each source, which is defined as a circle of radius $R_s = 2.4 \times \mathrm{FWHM}$ (with a minimum radius of 5 pixels). The FWHM is modeled as a function of the off-axis angle to reproduce the broadening of the point-spread function (PSF; see Giacconi et al. 2002). In each band, a detected source has a $\mathrm{S/N} \approx S/(S + 2B)^{1/2} > 2.1$ within the extraction area of the image. Here B represents the background counts found in an annulus with outer radius $R_s + 12''$ and an inner radius of $R_s + 2''$, after masking out other sources, rescaled to the extraction region. A final catalog is then produced matching the two. We stress that the condition of having $\mathrm{S/N} > 2.1$ from aperture photometry in the extraction area corresponds to a high significance detection (the faintest detected sources have more than 10 counts). Our catalogs typically include fewer than 5 spurious sources, as tested with simulations.

Aperture photometry was performed within R_s in the soft and hard bands separately. Simulations have shown that such measurements lead to an underestimate of the source count rates by approximately −4% (see Tozzi et al. 2001). We correct for such photometric bias before converting the count rates to energy fluxes. The conversion factors, listed in columns (2) and (3) of Table 3, are computed for each exposure at the aim points, using the response matrices and assuming an average photon index $\Gamma = 1.4$. These vary from field to field due to the different

TABLE 3
Chandra CONVERSION FACTORS AND FLUX LIMITS

Cluster (1)	Conversion Factor[a] (0.5–2 keV) ($\times 10^{-11}$ ergs s^{-1} cm^{-2} counts^{-1} s^{-1}) (2)	Conversion Factor[a] (2–10 keV) ($\times 10^{-11}$ ergs s^{-1} cm^{-2} counts^{-1} s^{-1}) (3)	Flux Limit (0.5–2 keV) ($\times 10^{-16}$ ergs s^{-1} cm^{-2}) (4)	Flux Limit (2–10 keV) ($\times 10^{-15}$ ergs s^{-1} cm^{-2}) (5)
RX J0152−1357	5.12	2.98	7.08	4.47
RX J0849+4452	4.92	2.96	1.67	1.00
RDCS J0910+5422	5.81	3.04	2.00	2.26
MS 1054−0321	3.42	2.82	2.82	2.51
RDCS J1252−2927	5.50	3.03	2.00	1.26

[a] The conversion factors are obtained for an average spectral slope of $\Gamma = 1.4$.

TABLE 4

OPTICAL AND X-RAY PROPERTIES OF *Chandra* SOURCES IN THE RX J0152−1357 ACS FIELD

Chandra ID (1)	R.A. (J2000.0) (2)	Decl. (J2000.0) (3)	z (4)	V_{625} (5)	i_{775} (6)	z_{850} (7)	HR (8)	$F_{0.5-2}$ (9)	F_{2-10} (10)	$L_{0.5-2}$ (11)	L_{2-10} (12)	Morphology (13)	Class (14)
16	01 52 54.45	−13 56 25.37	...	25.37 ± 0.06	24.79 ± 0.04	23.97 ± 0.03	0.97 ± 0.24	0.02427	9.309	...	...	...	...
19	01 52 49.37	−13 54 40.28	...	25.26 ± 0.03	24.88 ± 0.03	24.64 ± 0.04	−0.58 ± 0.18	2.892	4.486	...	...	...	...
23	01 52 43.79	−13 59 01.10	0.8201	20.46 ± 0.01	20.44 ± 0.01	20.22 ± 0.01	−0.62 ± 0.05	35.04	47.67	44.05	44.18	2	QSO 1
24[a]	01 52 41.56	−13 59 19.00	...	...	...	...	0.27 ± 0.16	2.152	22.01	...	...	...	...
25	01 52 40.95	−14 00 08.32	0.9934	22.17 ± 0.01	21.71 ± 0.01	21.26 ± 0.01	−0.56 ± 0.13	5.306	8.747	43.44	43.65	2	AGN 1
28	01 52 39.84	−13 57 40.80	0.8672	21.57 ± 0.01	20.87 ± 0.01	20.27 ± 0.01	−0.09 ± 0.07	18.21	89.39	43.83	44.52	2	QSO 2
29[b]	01 52 39.69	−13 55 24.73	...	25.60 ± 0.05	25.26 ± 0.04	24.70 ± 0.05	−0.35 ± 0.20	2.414	6.714	...	...	...	...
59	01 52 50.29	−13 54 44.23	1.3272	22.39 ± 0.01	21.98 ± 0.01	21.31 ± 0.01	−0.43 ± 0.37	0.7815	1.823	42.92	43.28	3	AGN 1
60	01 52 49.34	−13 56 57.70	...	28.06 ± 0.27	28.00 ± 0.26	27.20 ± 0.24	−0.65 ± 0.31	0.9875	1.227	...	...	...	...
62	01 52 47.62	−13 59 49.35	...	25.65 ± 0.06	25.25 ± 0.05	24.23 ± 0.03	−0.86 ± 0.21	1.822	0.8036	...	...	...	...
63	01 52 45.82	−13 55 28.41	0.57_{p}	22.84 ± 0.01	22.46 ± 0.01	22.31 ± 0.02	−0.74 ± 0.23	1.761	1.544	42.37	42.31	2	AGN 1
68	01 52 43.11	−13 55 19.69	1.18_{p}	24.29 ± 0.03	23.71 ± 0.02	22.94 ± 0.02	−0.59 ± 0.40	0.7663	1.156	42.78	42.96	...	AGN 1
83	01 52 42.80	−13 59 55.07	0.6400	22.00 ± 0.01	21.24 ± 0.01	20.86 ± 0.01	−0.57 ± 0.35	0.8252	1.300	42.16	42.36	2	AGN 1

NOTES.—Col. (1): Identification number from the *Chandra* catalog. Cols. (2) and (3): Barycentric coordinates of the source on the ACS images as determined with SExtractor. Units of right ascension are hours, minutes, and seconds, and units of declination are degrees, arcminutes, and arcseconds. Col. (4): Spectroscopic redshift z_{spec} or the BPZ photometric (denoted with the subscript "p") if z_{spec} is not available. Only the most reliable photometric redshifts (BPZ ODDS $\geq$0.9) are listed. See text for details. Cols. (5), (6), and (7): Isophotal magnitudes from SExtractor in the AB system. The magnitudes are corrected for Galactic extinction. Col. (8): X-ray hardness ratio. Cols. (9) and (10): Observed *Chandra* fluxes in the soft (0.5–2 keV) and hard (2–10 keV) bands in units of $\times 10^{-15}$ ergs s^{-1} cm^{-2}. Cols. (11) and (12): Base 10 logarithm of the observed X-ray luminosities in units of ergs s^{-1} in the soft and hard bands calculated with the cosmological parameters $(H_0,\ \Omega_m,\ \Omega_\Lambda) = (70,\ 0.3,\ 0.7)$. Col. (13): Visual classification of the galaxies into three general morphological types: (1) early-type, (2) late-type, (3) irregular/peculiar. Col. (14): X-ray class as in Szokoly et al. (2004).

[a] No optical counterpart is detected by SExtractor, although some very low-surface brightness material is observed within the error circle. The position of the X-ray peak after registration is listed.

[b] The X-ray peak is located approximately 0.9″ to the southeast of a resolved galaxy with a compact core. We list the properties of this galaxy in the table.

TABLE 5
OPTICAL AND X-RAY PROPERTIES OF *Chandra* SOURCES IN THE RX J0849+4452 ACS FIELD

Chandra ID	R.A. (J2000.0)	Decl. (J2000.0)	z	i_{775}	z_{850}	HR	$F_{0.5-2}$	F_{2-10}	$L_{0.5-2}$	L_{2-10}	Morphology	Class
37.....	08 49 14.66	44 52 31.63	...	23.33 ± 0.02	22.51 ± 0.02	0.44 ± 0.20	0.2200	3.445	...	...	2	...
41.....	08 49 13.69	44 52 38.14	...	23.18 ± 0.02	22.52 ± 0.01	1.00 ± 0.12	0	3.284	...	...	2	...
58[a]	08 49 06.08	44 50 38.19	...	25.69 ± 0.07	25.48 ± 0.07	0.63 ± 0.30	0.06530	1.741	...	...	...	...
60.....	08 49 05.33	44 52 03.76	...	23.52 ± 0.02	22.79 ± 0.01	0.53 ± 0.11	0.4689	9.206	...	...	1	...
67.....	08 49 03.97	44 50 24.64	...	23.11 ± 0.01	22.19 ± 0.01	0.22 ± 0.27	0.2077	1.961	...	...	3	...
78.....	08 48 58.71	44 50 34.81	...	20.88 ± 0.01	20.37 ± 0.01	0.17 ± 0.27	0.2119	1.786	...	...	1	...
84.....	08 48 56.78	44 52 26.32	1.3290	22.13 ± 0.01	21.88 ± 0.01	−0.47 ± 0.09	2.440	5.326	43.41	43.75	2	AGN 1
86.....	08 48 54.48	44 51 50.12	1.0350	20.77 ± 0.01	20.62 ± 0.01	−0.31 ± 0.06	4.878	15.33	43.44	43.94	1	QSO 1
88.....	08 48 53.90	44 53 52.13	0.7250	21.09 ± 0.01	20.68 ± 0.01	0.14 ± 0.16	0.5182	4.171	42.09	42.99	3	AGN 2
93.....	08 48 46.59	44 53 58.86	...	24.5 ± 0.2	27.2 ± 0.2	−0.36 ± 0.15	0.9238	2.607	...	...	...	...
102[b]	08 48 40.57	44 51 36.24	...	27.1 ± 0.1	26.8 ± 0.1	−0.31 ± 0.39	0.2150	0.6892	...	...	...	...
104.....	08 48 40.44	44 54 56.39	...	28.0 ± 0.2	27.5 ± 0.2	−0.71 ± 0.48	0.2903	0.2942	...	...	...	...
109.....	08 48 38.02	44 53 52.70	3.2880	25.12 ± 0.09	25.09 ± 0.09	0.01 ± 0.15	0.7686	4.763	43.87	44.66	...	QSO 2
116.....	08 48 36.35	44 52 51.85	1.1943	22.88 ± 0.01	22.34 ± 0.01	−0.44 ± 0.08	3.130	7.304	43.40	43.77	2	AGN 1
119.....	08 48 33.63	44 54 10.36	...	24.97 ± 0.06	24.73 ± 0.04	−0.39 ± 0.30	0.3250	0.8555	...	...	...	...
122.....	08 48 31.72	44 54 42.92	...	24.69 ± 0.03	24.07 ± 0.02	−0.08 ± 0.18	0.6031	3.126	...	...	1	...
124.....	08 48 31.61	44 53 44.00	0.5590	23.60 ± 0.01	23.44 ± 0.01	−0.72 ± 0.16	0.9245	0.9014	42.07	42.05	1	AGN 1
129.....	08 48 27.50	44 56 05.96	...	23.77 ± 0.02	23.34 ± 0.02	0.19 ± 0.15	0.5864	5.187	...	...	2	...
130.....	08 48 27.35	44 54 34.79	0.8990	20.35 ± 0.01	20.13 ± 0.01	−0.46 ± 0.06	4.789	10.79	43.28	43.64	3	AGN 1
133.....	08 48 24.74	44 53 55.28	0.7470	21.72 ± 0.01	21.39 ± 0.01	−0.02 ± 0.18	0.5844	3.364	42.17	42.93	2	AGN 2
136.....	08 48 23.76	44 54 24.94	...	22.75 ± 0.01	22.19 ± 0.01	0.64 ± 0.28	0.07635	2.108	...	...	2	...
178.....	08 48 50.67	44 51 49.32	1.0700	22.13 ± 0.01	21.47 ± 0.01	−0.92 ± 0.72	0.1671	0.04170	42.01	41.41	2	AGN 1
184.....	08 48 50.48	44 53 07.93	...	19.92 ± 0.01	19.48 ± 0.01	−1.00 ± 0.46	0.2928	0	...	...	2	...
194.....	08 48 49.53	44 54 27.30	...	21.24 ± 0.01	20.92 ± 0.01	1.00 ± 0.71	0	1.273	...	...	2	...

NOTE.—Units of right ascension are hours, minutes, and seconds, and units of declination are degrees, arcminutes, and arcseconds. Morphological notation is as in Table 4.

[a] The X-ray emission coincides with an extended low surface brightness patch. There is a brighter ($i_{775} = 23.9$), compact source ~1.7″ to the southwest.

[b] The X-ray emission is extended and overlaps a faint optical source whose properties we list here.

calibration and the different Galactic absorption, which is small along the line of sight to the five clusters ($N_{\rm H} \approx 2 \times 10^{20}$–$6 \times 10^{20}$ cm^{-2}) and therefore amounts to corrections of only a few percent in the soft band and essentially none in the hard band. We quote the hard fluxes in the canonical 2–10 keV band, as extrapolated from counts measured from the 2–7 keV band, in order to have a direct comparison with previous results.

Before computing the energy fluxes, the count rates were corrected for vignetting and converted to the count rates that would have been measured if the source were at the aim point. The correction is simply given by the ratio of the value of the exposure map at the aim point to the value of the exposure map at the source position. This is done separately for the soft and the hard bands, using the exposure maps computed for energies of 1.5 and 4.5 keV. This procedure also accounts for variations of effective exposure time across the field of view due to missing columns and gaps within the CCD. The flux limits derived for each field when the sky coverage approaches zero are listed in columns (3) and (4) of Table 3. To minimize spurious detections, sources with both soft and hard fluxes below these detection thresholds are not considered in the following.

2.3. *Image Registration and Optical Identifications*

To identify the optical candidates, the X-ray images were registered to the same scale and orientation as the ACS detection images. Because of the significantly lower spatial resolution of

TABLE 6
OPTICAL AND X-RAY PROPERTIES OF *Chandra* SOURCES IN THE RDCS J0910+5422 ACS FIELD

Chandra ID	R.A. (J2000.0)	Decl. (J2000.0)	z	i_{775}	z_{850}	HR	$F_{0.5-2}$	F_{2-10}	$L_{0.5-2}$	L_{2-10}	Morphology	Class
38.....	09 10 57.04	54 23 43.47	...	22.40 ± 0.02	22.32 ± 0.02	−0.52 ± 0.08	3.834	6.279	...	...	1	...
40.....	09 10 53.88	54 22 37.64	...	26.4 ± 0.1	26.2 ± 0.1	−0.08 ± 0.26	0.4382	1.954	...	...	...	...
46.....	09 10 50.90	54 22 54.10	...	24.06 ± 0.02	23.96 ± 0.02	−0.28 ± 0.44	0.2333	0.6797	...	...	2	...
51.....	09 10 48.26	54 22 30.23	1.1110	23.30 ± 0.02	22.53 ± 0.01	−0.46 ± 0.33	0.4078	0.7884	42.44	42.73	1	AGN 1
54.....	09 10 47.67	54 22 13.62	...	22.30 ± 0.01	21.65 ± 0.01	−0.45 ± 0.19	0.8900	1.747	...	...	2	...
65.....	09 10 43.26	54 21 51.71	1.1040	23.48 ± 0.02	22.70 ± 0.01	0.19 ± 0.37	0.2249	1.735	42.18	43.06	1	AGN 2
66.....	09 10 42.78	54 20 37.04	...	22.19 ± 0.01	21.56 ± 0.01	0.10 ± 0.29	0.2684	1.698	...	...	2	...
69[a]	09 10 42.03	54 22 29.42	...	...	...	−0.60 ± 0.49	0.2697	0.3478	...	...	...	...
70.....	09 10 42.01	54 21 29.58	...	21.18 ± 0.01	20.95 ± 0.01	−0.44 ± 0.14	1.254	2.553	...	...	1	...
71[b]	09 10 41.99	54 23 42.50	...	22.84 ± 0.01	22.90 ± 0.01	−0.41 ± 0.06	5.652	12.28	...	...	...	...
76.....	09 10 40.16	54 23 02.35	...	20.71 ± 0.01	20.57 ± 0.01	−0.14 ± 0.15	1.024	4.036	...	...	2	...

NOTE.—Units of right ascension are hours, minutes, and seconds, and units of declination are degrees, arcminutes, and arcseconds. Morphological notation is as in Table 4.

[a] Saturated unresolved source.

[b] The optical source appears unresolved but possibly imbedded in a compact, faint nebulosity.

TABLE 7

OPTICAL AND X-RAY PROPERTIES OF *Chandra* SOURCES IN THE MS 1054−0321 ACS FIELD

Chandra ID	R.A. (J2000.0)	Decl. (J2000.0)	z	V_{606}	i_{775}	z_{850}	HR	$F_{0.5-2}$	F_{2-10}	$L_{0.5-2}$	L_{2-10}	Morphology	Class
5	10 57 10.58	−03 36 10.46	1.06_{p}	24.73 ± 0.06	24.56 ± 0.04	23.85 ± 0.03	−0.72 ± 0.27	0.7048	0.9319	42.63	42.75	...	AGN 1
8	10 57 08.50	−03 36 11.51	...	25.46 ± 0.03	...	...	−0.55 ± 0.08	4.744	11.52	...	...	3	...
13[a]	10 57 05.55	−03 35 50.45	...	22.86 ± 0.01	22.81 ± 0.01	22.76 ± 0.02	−0.57 ± 0.10	3.146	7.154	...	...	...	...
15	10 57 05.13	−03 35 41.87	1.02_{p}	22.69 ± 0.01	21.88 ± 0.01	21.29 ± 0.01	−0.63 ± 0.07	5.041	9.551	43.44	43.72	1	AGN 1
16	10 57 04.90	−03 38 20.76	...	26.23 ± 0.09	26.15 ± 0.08	25.51 ± 0.08	0.95 ± 0.27	0.02119	6.945	...	...	...	...
20	10 57 02.70	−03 39 43.98	0.73_{p}	23.18 ± 0.03	22.56 ± 0.01	22.03 ± 0.01	0.03 ± 0.18	0.7993	7.031	42.28	43.23	3	AGN 2
22	10 57 02.27	−03 41 00.41	...	25.05 ± 0.04	...	...	−0.81 ± 0.35	0.5444	0.4700	...	...	...	...
25	10 57 00.08	−03 34 46.09	1.1770	21.76 ± 0.01	21.56 ± 0.01	21.48 ± 0.01	−0.46 ± 0.11	2.697	8.232	43.32	43.81	1	AGN 1
26	10 57 00.02	−03 35 12.92	0.2500	18.08 ± 0.01	17.78 ± 0.01	17.66 ± 0.01	−0.68 ± 0.44	0.3814	0.6024	40.86	41.06	2	Galaxy
30	10 56 58.81	−03 38 51.11	...	22.87 ± 0.01	22.41 ± 0.01	22.15 ± 0.01	−0.39 ± 0.04	15.28	55.69	...	...	3	...
32	10 56 56.34	−03 36 36.20	...	25.38 ± 0.05	25.34 ± 0.05	24.59 ± 0.06	−0.18 ± 0.40	0.3739	2.121	...	...	...	...
33	10 56 56.32	−03 39 29.85	...	26.03 ± 0.07	25.74 ± 0.06	25.08 ± 0.06	−0.66 ± 0.42	0.4455	0.7518	...	...	...	...
40	10 56 52.64	−03 38 19.87	...	22.89 ± 0.02	22.47 ± 0.01	22.27 ± 0.01	−0.48 ± 0.18	1.190	3.462	...	...	2	...
41	10 56 51.42	−03 38 00.62	1.17_{p}	24.00 ± 0.04	23.54 ± 0.02	22.76 ± 0.02	−0.58 ± 0.28	0.5931	1.291	42.66	43.00	2	AGN 1
44	10 56 50.65	−03 35 08.56	0.8180	22.19 ± 0.01	21.32 ± 0.01	20.96 ± 0.01	−0.77 ± 0.06	6.891	7.279	43.34	43.36	1	AGN 1
48	10 56 48.99	−03 38 33.35	...	23.5 ± 0.1	25.1 ± 0.1	24.3 ± 0.1	−0.45 ± 0.33	0.4747	1.486	...	...	...	...
49	10 56 48.87	−03 37 25.88	0.1818	17.79 ± 0.01	17.19 ± 0.01	16.89 ± 0.01	−0.61 ± 0.12	2.106	4.215	41.29	41.59	1	Galaxy
57	10 56 44.34	−03 38 06.79	1.12_{p}	25.41 ± 0.06	24.94 ± 0.04	24.28 ± 0.04	0.27 ± 0.35	0.2381	3.407	42.22	43.37	...	AGN 2
59	10 56 43.69	−03 37 32.46	1.08_{p}	23.89 ± 0.04	23.52 ± 0.02	22.77 ± 0.02	−0.17 ± 0.32	0.4240	2.470	42.43	43.19	3	AGN 2
86	10 57 04.26	−03 39 47.18	...	23.63 ± 0.02	23.40 ± 0.02	22.97 ± 0.02	0.75 ± 0.36	0.05844	3.374	...	...	1	...
87	10 57 02.15	−03 34 52.67	1.04_{p}	24.62 ± 0.05	24.26 ± 0.03	23.69 ± 0.03	0.37 ± 0.38	0.1803	3.241	42.02	43.27	...	AGN 2
88[b]	10 56 56.40	−03 36 44.11	0.4581	20.10 ± 0.01	19.20 ± 0.01	18.83 ± 0.01	0.21 ± 0.34	0.3729	4.712	41.46	42.56	2	AGN 2
94	10 56 50.89	−03 35 04.37	...	21.59 ± 0.01	20.71 ± 0.01	20.33 ± 0.01	−0.69 ± 0.15	1.616	2.417	...	...	1	...
102[c]	10 57 00.96	−03 39 18.04	...	...	...	...	−0.54 ± 0.48	0.3167	0.7836	...	...	...	...

NOTE.—Units of right ascension are hours, minutes, and seconds, and units of declination are degrees, arcminutes, and arcseconds. Morphological notation is as in Table 4.

[a] The optical source appears unresolved but possibly imbedded in a compact, faint nebulosity.

[b] The X-ray emission consists of two peaks aligned along a north-south axis and separated by $\approx 4''$. The northern peak coincides with a large spiral galaxy whose properties we list here.

[c] No optical counterpart is detected in the ACS detection image. The position of the X-ray peak after registration is listed.

TABLE 8

OPTICAL AND X-RAY PROPERTIES OF *Chandra* SOURCES IN THE RDCS J1252−2927 ACS FIELD

Chandra ID	R.A. (J2000.0)	Decl. (J2000.0)	z	i_{775}	z_{850}	HR	$F_{0.5-2}$	F_{2-10}	$L_{0.5-2}$	L_{2-10}	Morphology	Class
94[a]	12 53 03.98	−29 28 25.67	...	...	...	−0.20 ± 0.28	0.3483	1.277	...	...	...	...
95	12 53 03.89	−29 27 58.70	...	23.90 ± 0.03	23.28 ± 0.02	−0.21 ± 0.25	0.4088	1.479	...	...	1	...
96	12 53 03.64	−29 27 42.13	...	20.54 ± 0.01	20.12 ± 0.01	−0.34 ± 0.31	0.3310	0.9028	...	...	2	...
97	12 53 03.60	−29 28 28.43	0.4762	20.38 ± 0.01	20.01 ± 0.01	0.07 ± 0.12	1.078	6.831	41.96	42.77	2	AGN 2
100	12 53 01.50	−29 25 38.76	0.7465	20.59 ± 0.01	20.33 ± 0.01	−0.50 ± 0.05	14.31	26.42	43.56	43.83	2	QSO 1
102[b]	12 53 01.08	−29 27 34.25	...	...	...	−1.00 ± 0.11	0.8949	0	...	...	...	...
105[c]	12 53 00.69	−29 25 36.63	...	25.13 ± 0.03	25.11 ± 0.04	−0.65 ± 0.43	0.3757	0.4351	...	...	...	...
107	12 53 00.39	−29 29 17.15	...	22.12 ± 0.01	21.60 ± 0.01	−0.19 ± 0.08	2.884	10.71	...	...	2	...
108	12 52 59.93	−29 25 18.44	1.1761	23.50 ± 0.02	22.80 ± 0.01	−0.15 ± 0.17	1.125	4.548	42.94	43.55	2	AGN 2
110	12 52 59.39	−29 27 03.24	0.070_{p}	19.87 ± 0.01	19.84 ± 0.01	−0.66 ± 0.39	0.3226	0.3612	39.59	39.63	3	Galaxy
115	12 52 58.14	−29 26 49.34	0.4694	20.13 ± 0.01	19.73 ± 0.01	−0.11 ± 0.22	0.5070	2.253	41.62	42.27	2	AGN 2
117	12 52 57.96	−29 27 57.11	...	23.25 ± 0.01	22.96 ± 0.01	0.24 ± 0.19	0.4021	3.637	...	...	2	...
119	12 52 56.86	−29 28 01.49	...	18.36 ± 0.01	18.04 ± 0.01	−0.35 ± 0.13	1.219	3.217	...	...	1	...
122	12 52 53.00	−29 26 14.10	...	24.76 ± 0.02	24.70 ± 0.02	−0.19 ± 0.20	0.6700	2.517	...	...	...	...
125	12 52 51.79	−29 28 09.11	...	25.07 ± 0.05	25.06 ± 0.04	1.00 ± 0.36	0	1.426	...	...	...	...
130	12 52 50.08	−29 27 00.74	1.5217	23.42 ± 0.01	23.02 ± 0.01	−0.43 ± 0.12	1.614	3.544	43.38	43.72	1	AGN 1
131	12 52 49.82	−29 27 54.88	1.2398	23.54 ± 0.02	23.31 ± 0.02	0.20 ± 0.31	0.1924	1.576	42.23	43.15	3	AGN 2
140	12 52 45.86	−29 28 51.73	...	23.69 ± 0.01	23.51 ± 0.01	0.60 ± 0.30	0.09044	1.972	...	...	1	...
142[d]	12 52 45.89	−29 29 04.00	...	20.92 ± 0.01	20.51 ± 0.01	0.12 ± 0.28	0.2564	1.791	...	...	1	...
144	12 52 44.48	−29 27 29.71	...	24.53 ± 0.03	24.01 ± 0.02	0.33 ± 0.10	1.066	11.70	...	...	2	...
146	12 52 42.48	−29 27 03.03	0.8440	20.91 ± 0.01	20.41 ± 0.01	−0.41 ± 0.30	0.4151	0.9540	42.15	42.52	1	AGN 1
147[e]	12 52 41.12	−29 29 11.47	...	22.26 ± 0.01	21.74 ± 0.01	−0.33 ± 0.15	1.008	2.820	...	...	3	...
148[f]	12 52 40.36	−29 27 14.13	1.3479	24.17 ± 0.03	23.57 ± 0.02	0.72 ± 0.15	0.1639	5.564	42.25	43.78	1	AGN 2
169	12 52 54.55	−29 27 50.15	...	23.53 ± 0.04	23.26 ± 0.04	0.41 ± 0.21	0.2776	3.696	...	...	2	...
175	12 53 02.39	−29 24 52.43	...	22.25 ± 0.01	22.24 ± 0.01	−0.46 ± 0.49	0.2524	0.5157	...	...	3	...
202[g]	12 52 59.51	−29 24 53.51	...	...	...	0.39 ± 0.49	0.1181	1.489	...	...	...	...

NOTE.—Units of right ascension are hours, minutes, and seconds, and units of declination are degrees, arcminutes, and arcseconds. Morphological notation is as in Table 4.

[a] No optical counterpart is detected in the ACS detection image. The peak X-ray position after registration is listed.

[b] Saturated unresolved source.

[c] There are two compact optical sources separated by 0.3″. We list the properties of the northwest source, which is the brightest of the two in our detection image.

[d] The X-ray emission is weak and extended and covers two sources, a large, smooth spheroid listed in the table and a smaller spheroid located 1.9″ to the southwest.

[e] The X-ray emission extends over a highly disturbed system that appears to consist of two merging galaxies. We list the properties of the southwest galaxy, the brightest and most extended of the two.

[f] Because the X-ray emission is extended, there is possible confusion in the optical identification between the compact galaxy listed in the table and a more diffuse and dimmer galaxy 0.8″ to the northwest.

[g] The X-ray peak, whose coordinates are listed here after registration, is located between a compact source ($i_{775} \approx 24.5$) at R.A. (J2000.0) = $12^{h}52^{m}59.61^{s}$ and decl. (J2000.0) = −29°24′52.6″ and several diffuse sources.

the *Chandra* data, only the brightest and most compact X-ray sources were used as reference points to ensure accurate matching of the centroids. Typically, this resulted in a list of ∼10 reference sources per field. The conversion between the two coordinate systems was performed with the `geomap` task in PyRAF, and the images and positions were transformed with `geotran` and `geoxytran` respectively. We find that a linear transformation is sufficient; polynomials of higher order do not show significant differences in the registration and may in fact give worse matches in regions where there is a deficit or a nonuniform distribution of reference points, such as near the edges. The errors in the astrometric solutions only apply to the fitted points and are very small (1–2 pixels). But from visual inspection, uncertainties of approximately 1″ are more realistic and may be slightly larger in the corners or extreme edges of the images. We therefore choose an error circle of 1″ in diameter and a positive identification of the optical candidate is made when an object is located within this error circle or nearest to it.

3. RESULTS

The optical counterparts and their global properties are listed in Tables 4, 5, 6, 7, and 8. A total of 98 X-ray sources fall in the ACS mosaics. We follow the recipe of Szokoly et al. (2004) to separate the X-ray sources into AGN and QSO classes, based on their total X-ray luminosities and hardness ratios. The classes are listed in the last column of each tables. In Figures 1, 2, 3, 4, and 5, the ACS detection image with superimposed X-ray contours, the $i - z$ color map, and the surface brightness (SB) profiles calculated with the PyRAF task `ellipse` are shown for each candidate. Only the detection image, marked with the position of the X-ray peak, is displayed if the optical source is too faint and/or diffuse to generate reliable color maps and SB profiles. At the depth of the images, optical counterparts are unequivocally identified for ∼96% of the X-ray sources. Uncertainty in the identification of the other 4% can be attributed to source confusion. In the following, we discuss the X-ray excess in the *Chandra* fields, the properties of the host galaxies and nuclei of the X-ray–selected AGNs, their environment and location in the ACS fields, the blue cores in the early types, and the cluster membership of some of the sources.

3.1. *The* $\log N(>S)-\log S$ *Relations*

It is customary to test for an overdensity of X-ray sources in the direction of clusters by comparing their cumulative number counts to those in a cluster-free background (e.g., Cappi et al. 2001; Molnar et al. 2002; Sun & Murray 2002). Any observed excess can presumably be attributed to sources associated with the cluster. Other possibilities, such as cosmic variance and

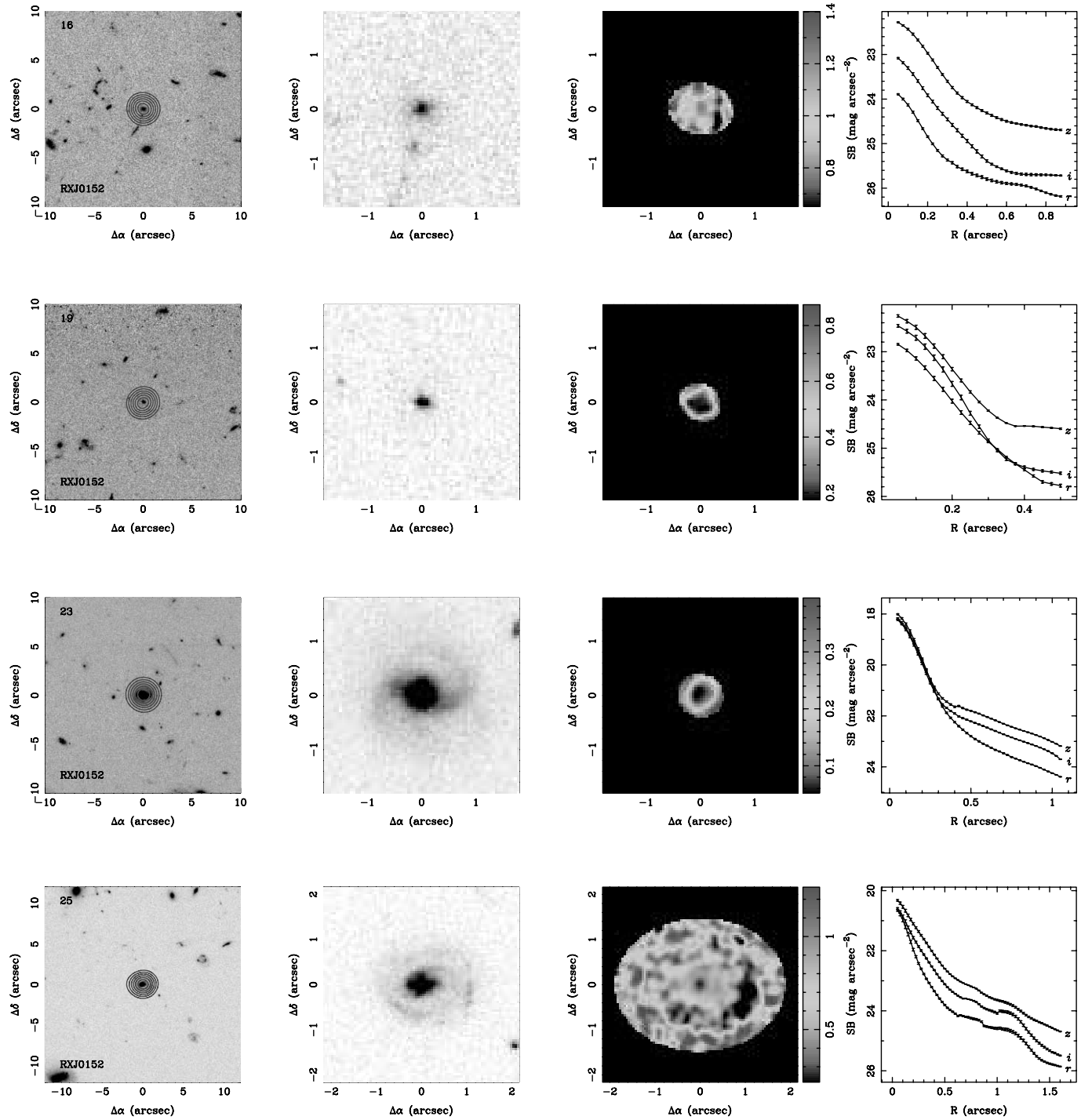

FIG. 1.—Optical candidates to the X-ray sources in the field of RX J0152−1357. *First panel*: The ACS detection image is centered on the nearest optical candidate. The ID number from the X-ray catalog is given in the top left corner and the abbreviated cluster name in the bottom left corner. Six X-ray contours, equally spaced between the minimum and maximum values in the cutout, are overlaid on the image. *Second panel*: Enlargement of the first panel. *Third panel*: The $i - z$ color map is displayed after smoothing with a 1.5 pixel wide Gaussian. The PSFs of the images were matched before combining them. The outer ellipse is defined by the Petrosian radius. *Fourth panel*: The surface brightness profiles are plotted along the fitted elliptical major axes. For nondetections or for optical sources that are too faint and diffuse for reliable color maps and SB profiles, only the detection image is displayed with a cross marking the location of the X-ray peak. [*See the electronic edition of the Supplement for a color version of this figure.*]

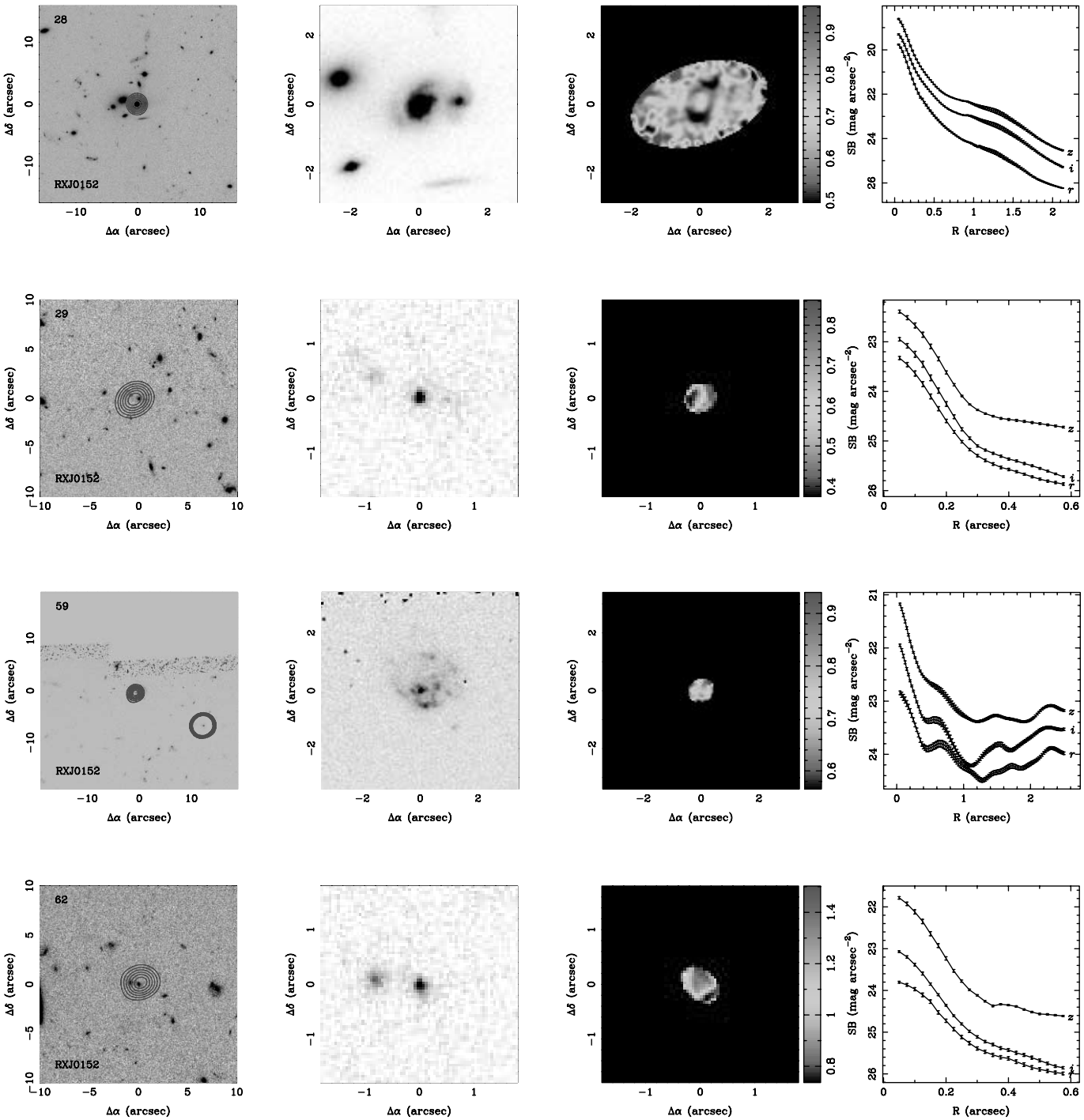

FIG. 1.—*Continued*

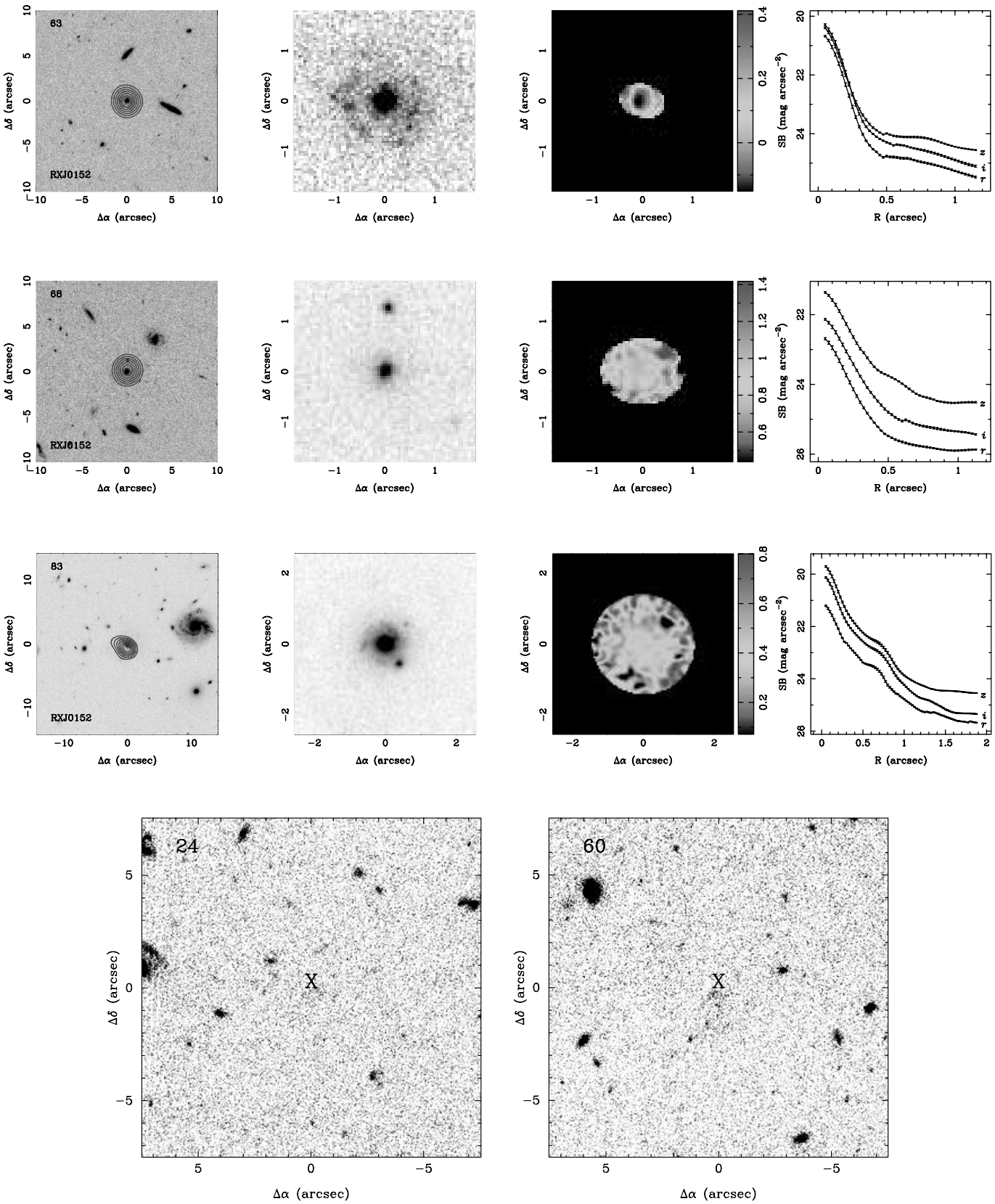

FIG. 1.—*Continued*

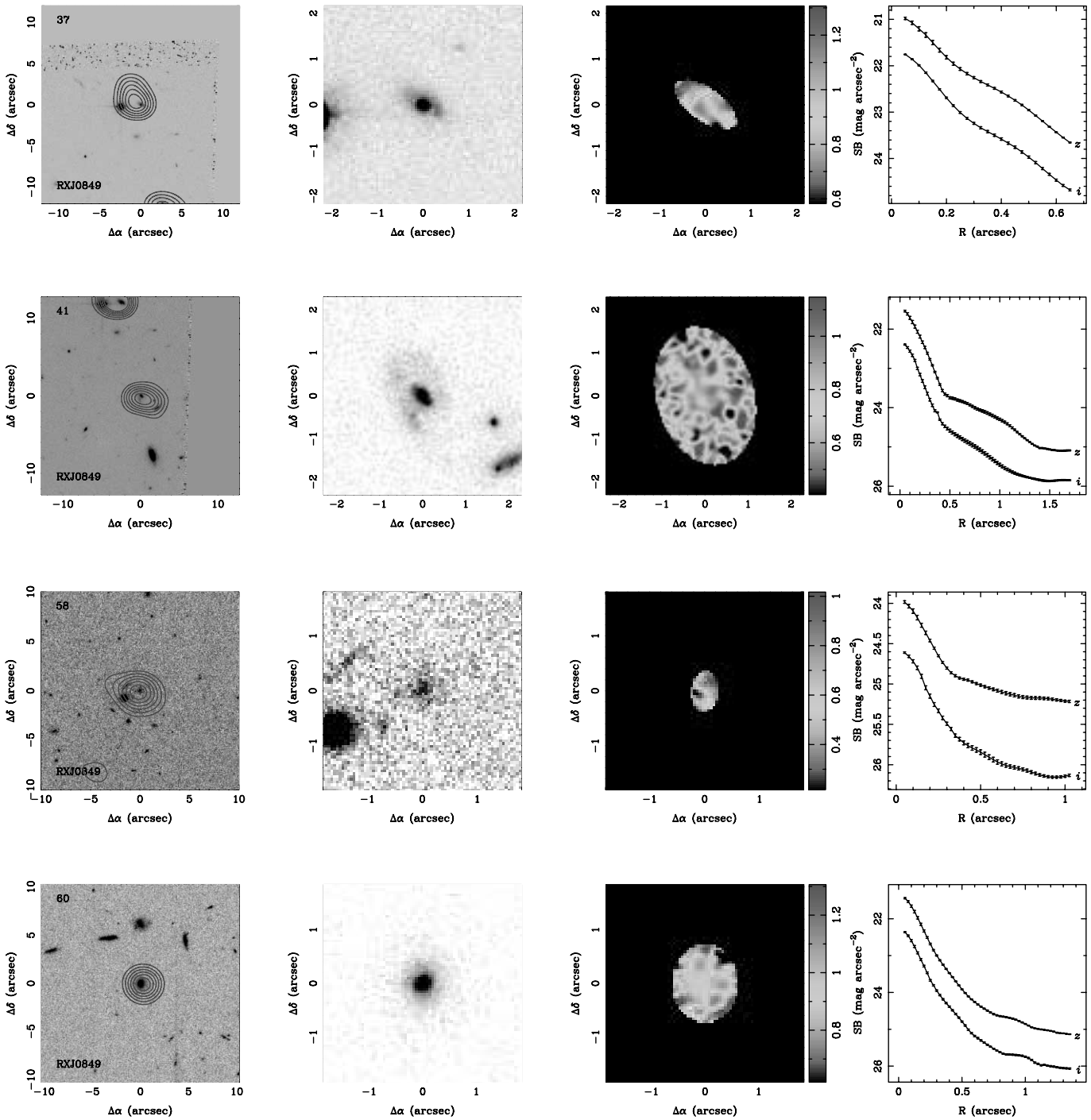

FIG. 2.—Same as Fig. 1, but for RX J0849+4452. [*See the electronic edition of the Supplement for a color version of this figure.*]

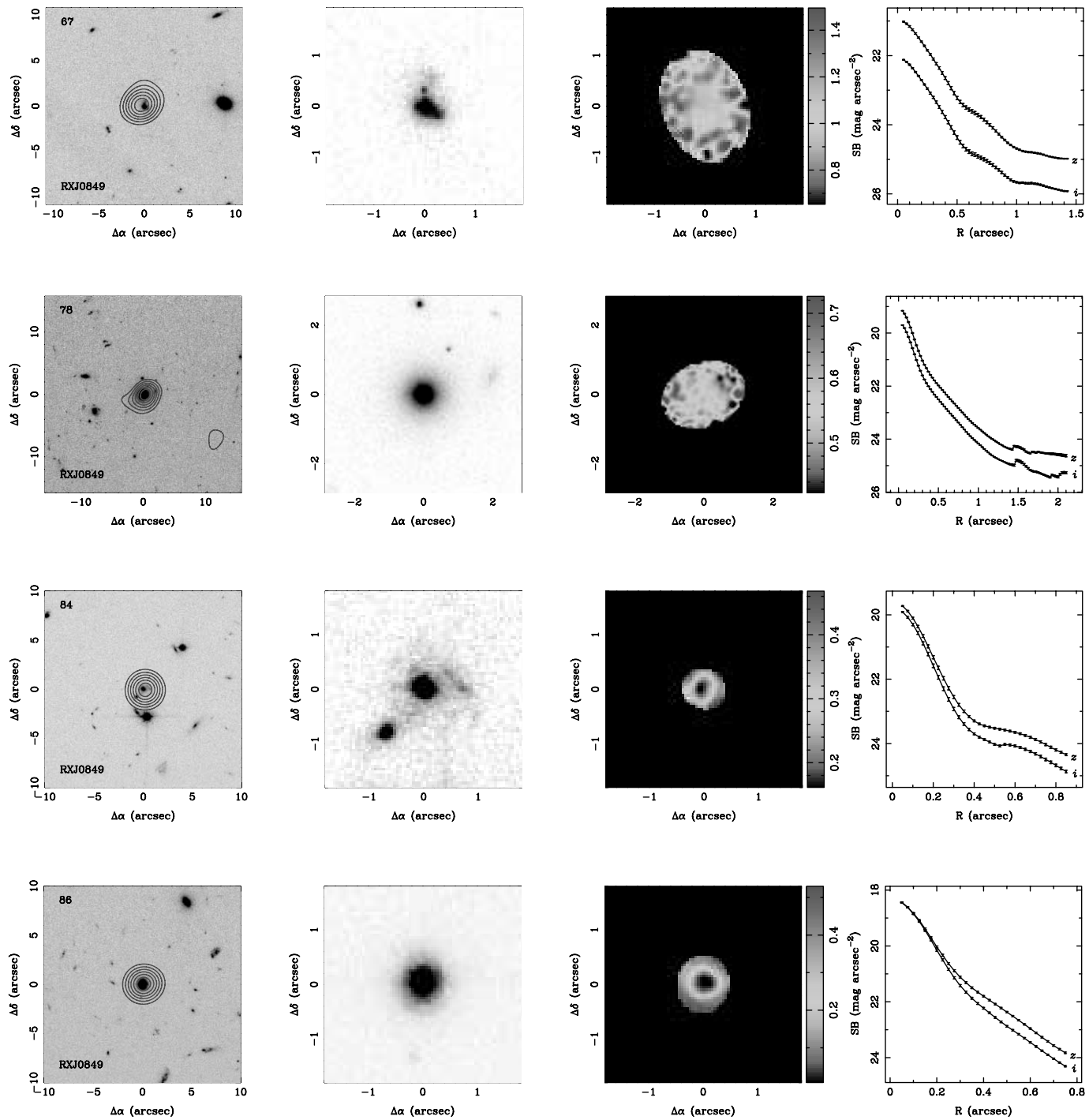

FIG. 2.—*Continued*

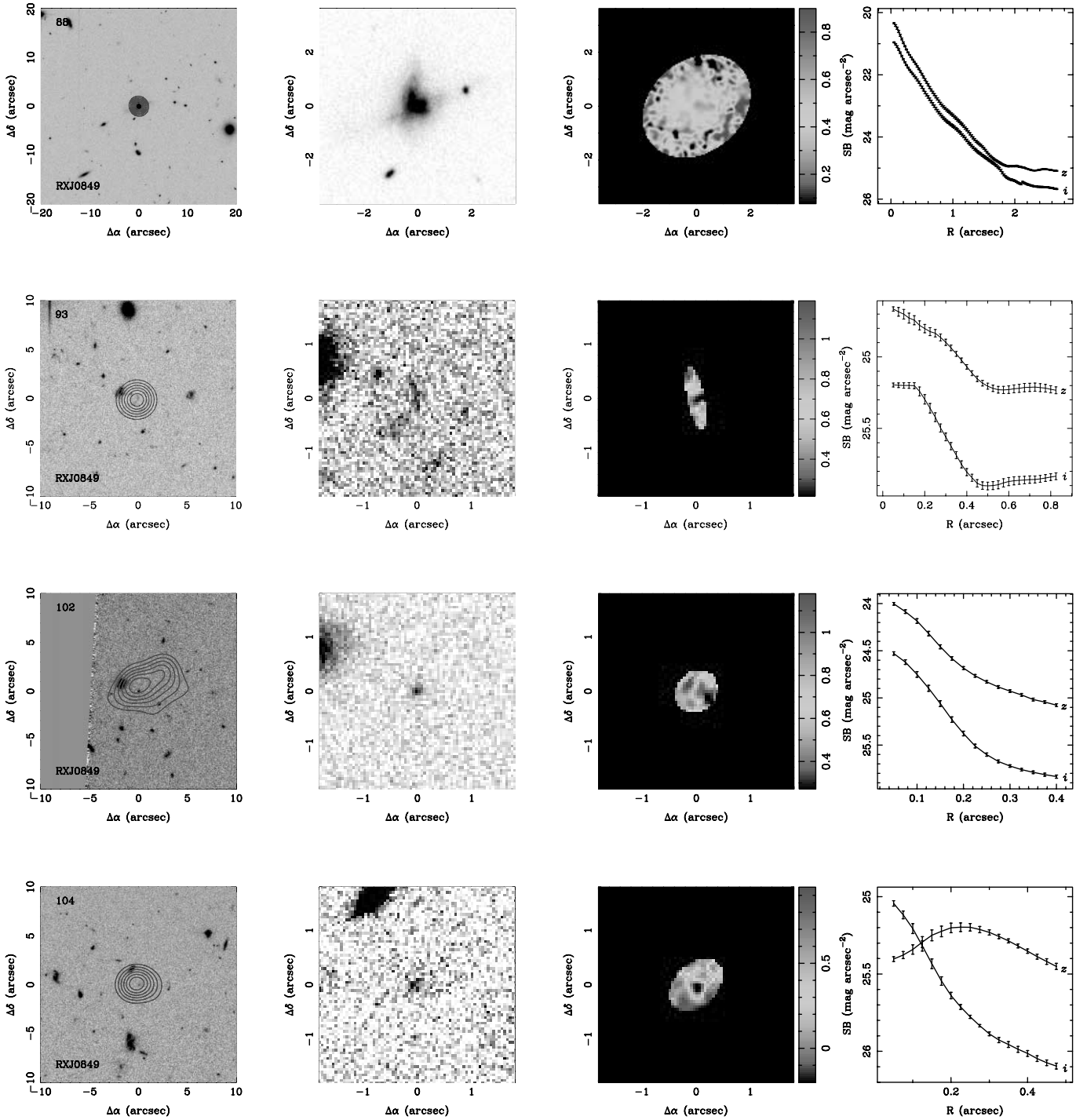

FIG. 2.—*Continued*

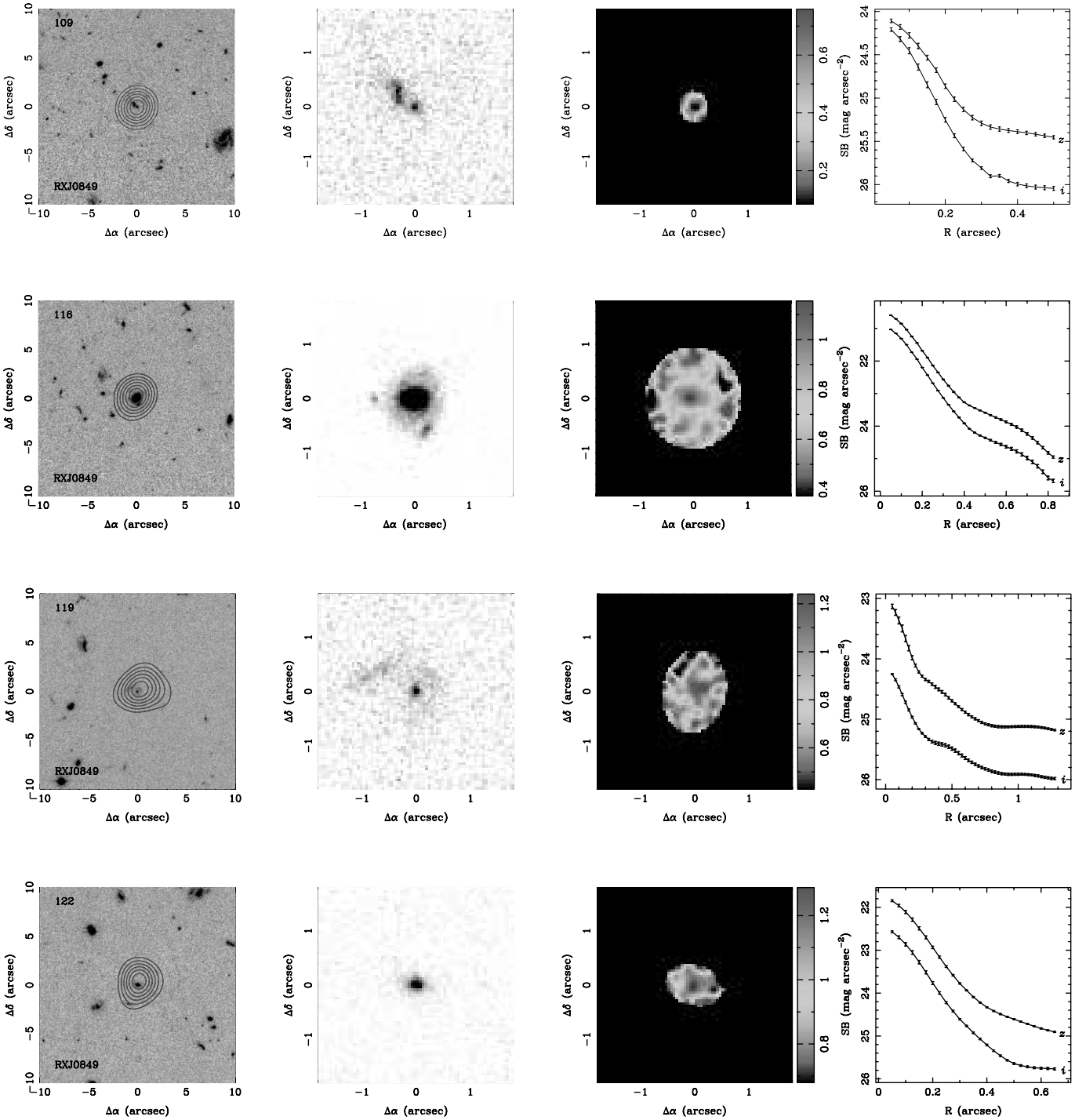

FIG. 2.— *Continued*

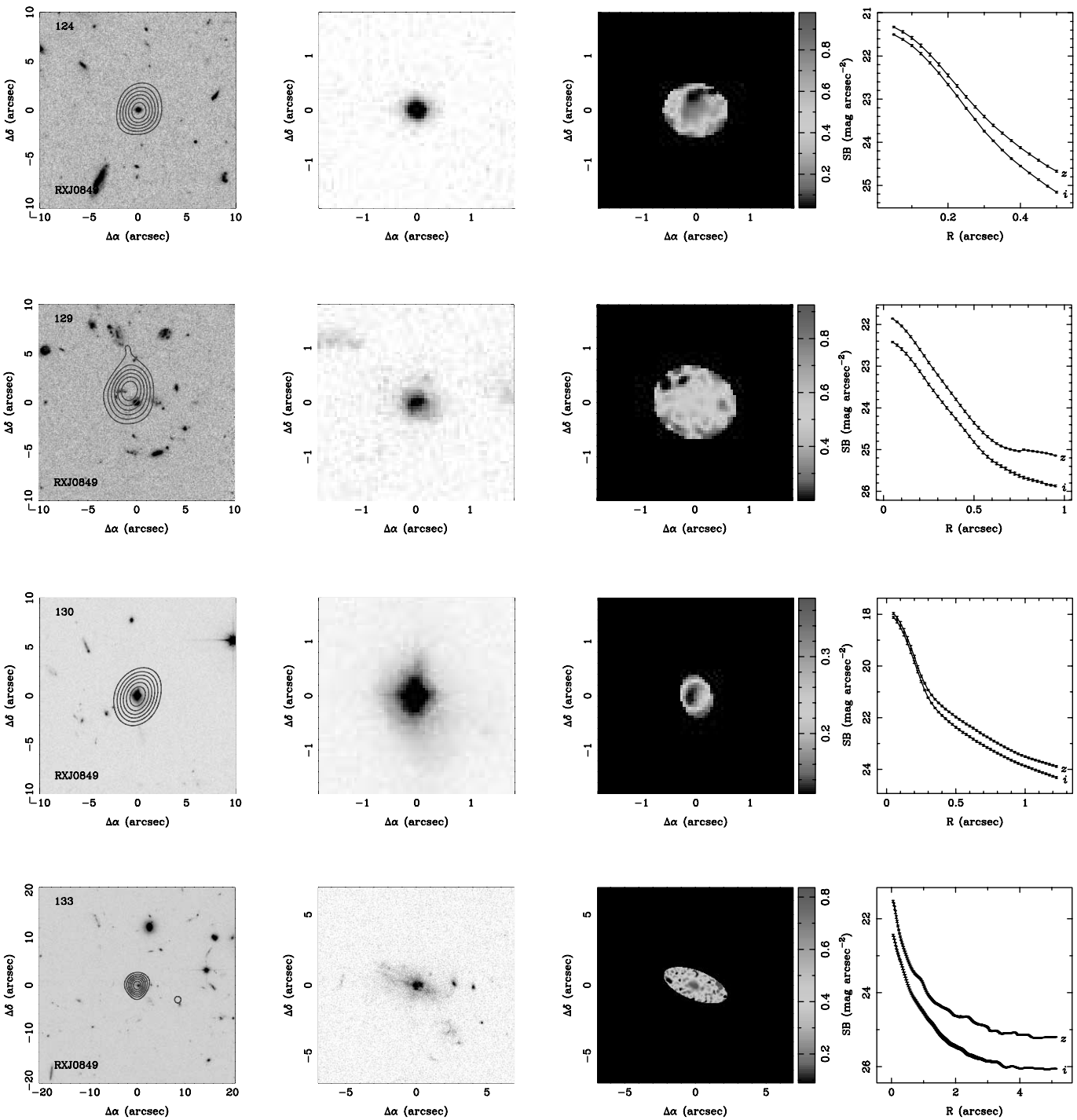

FIG. 2.—*Continued*

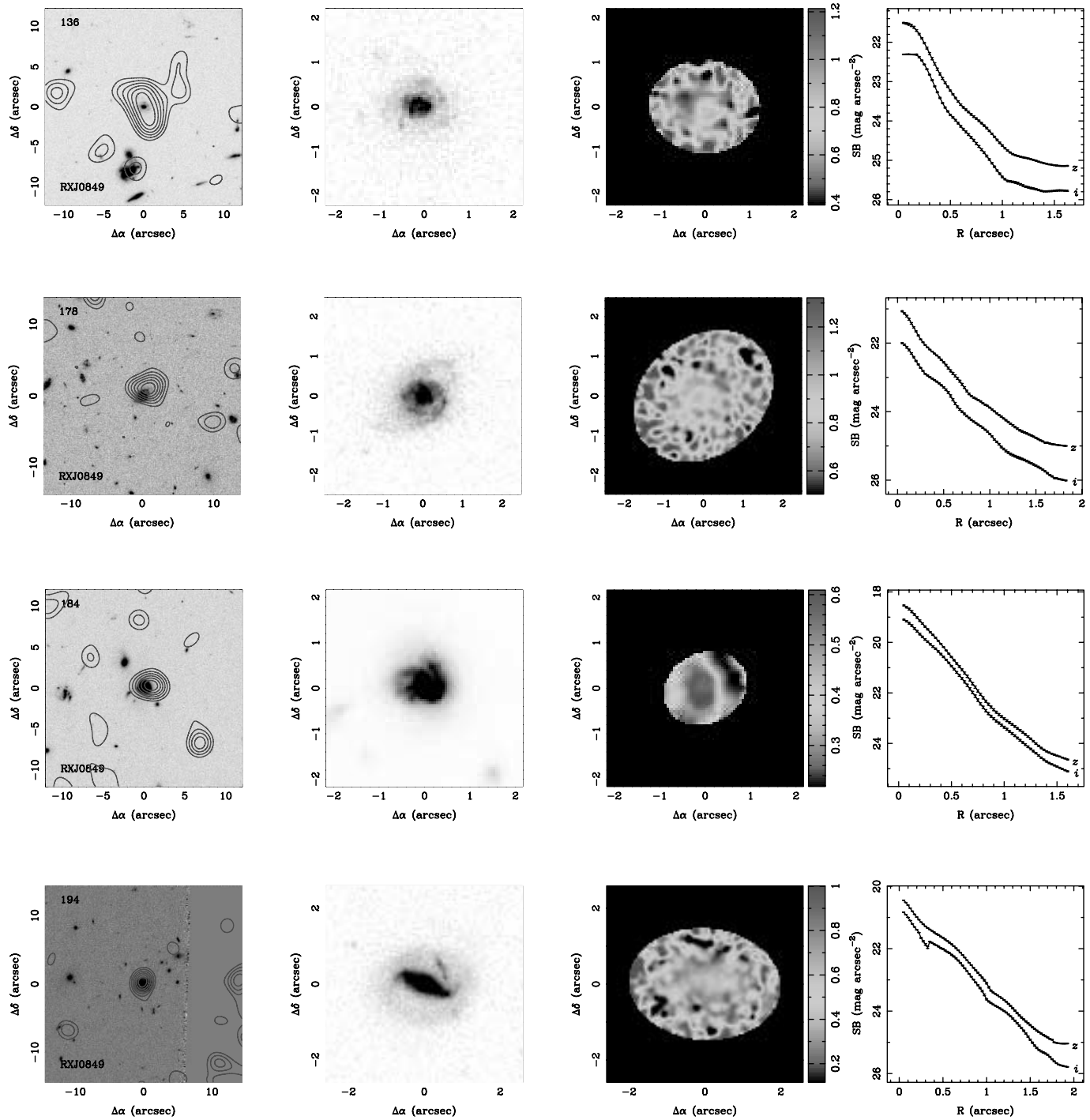

FIG. 2.— *Continued*

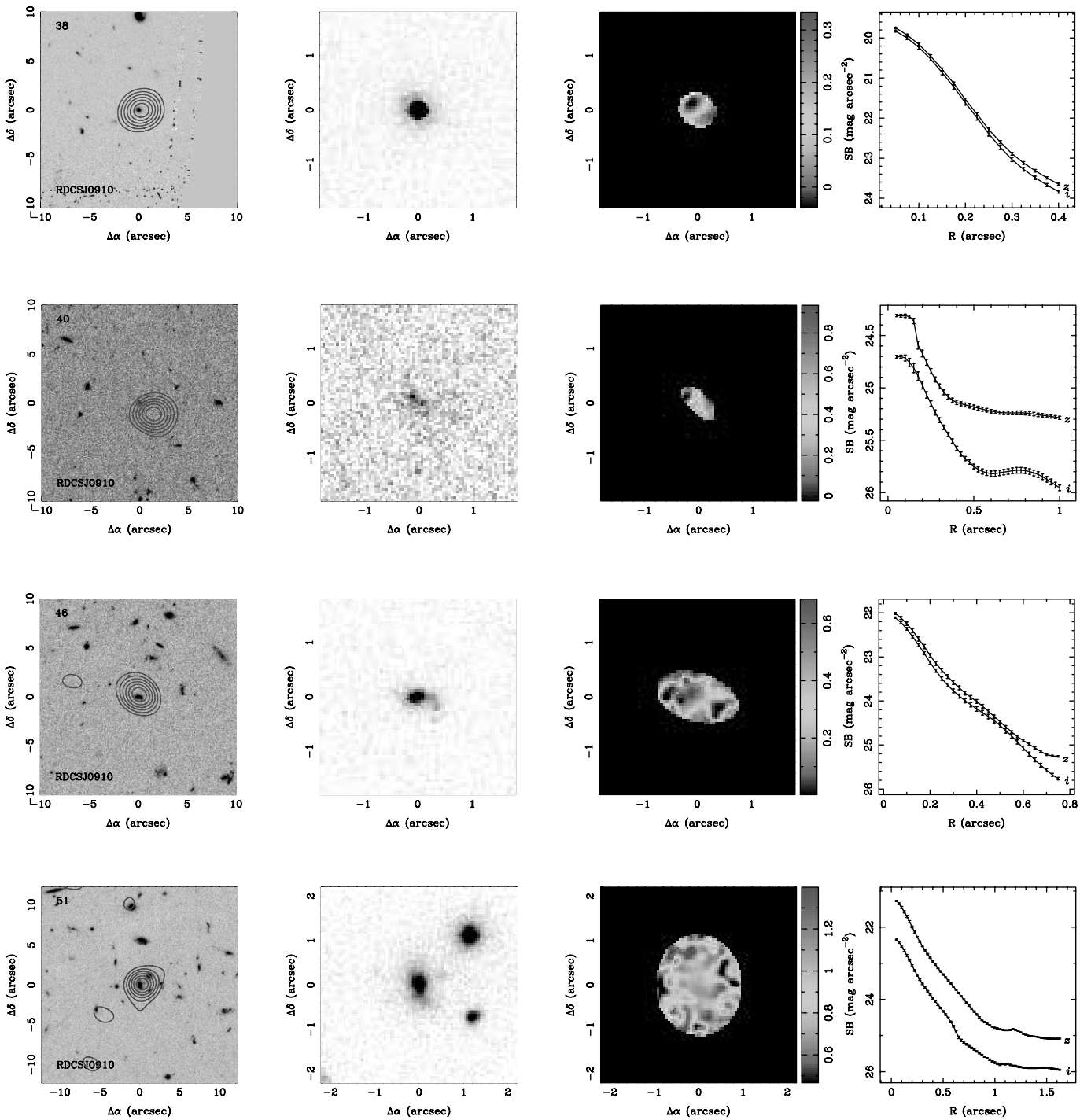

FIG. 3.—Same as Fig. 1, but for RDCS J0910+5422. [*See the electronic edition of the Supplement for a color version of this figure.*]

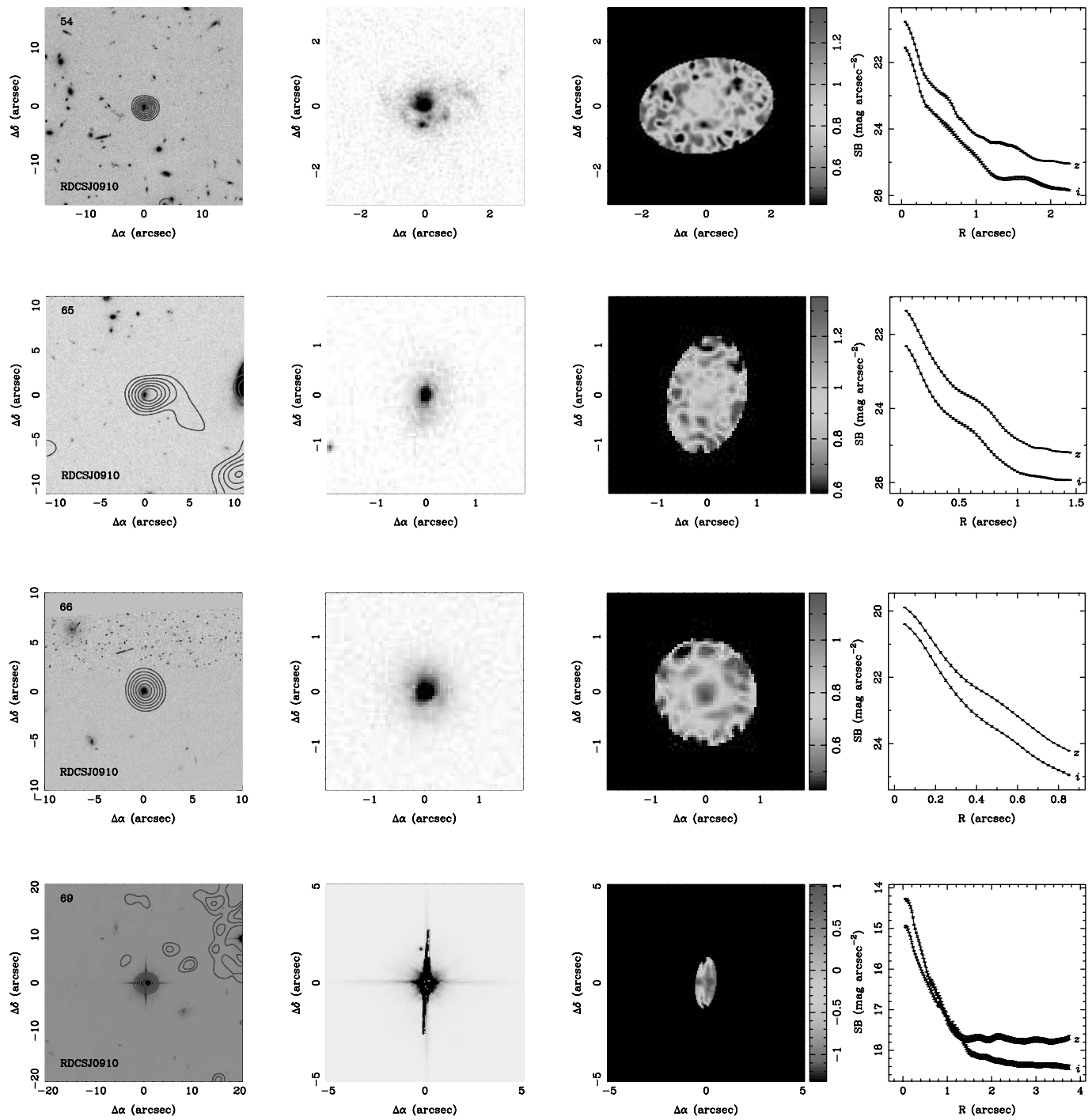

FIG. 3.— *Continued*

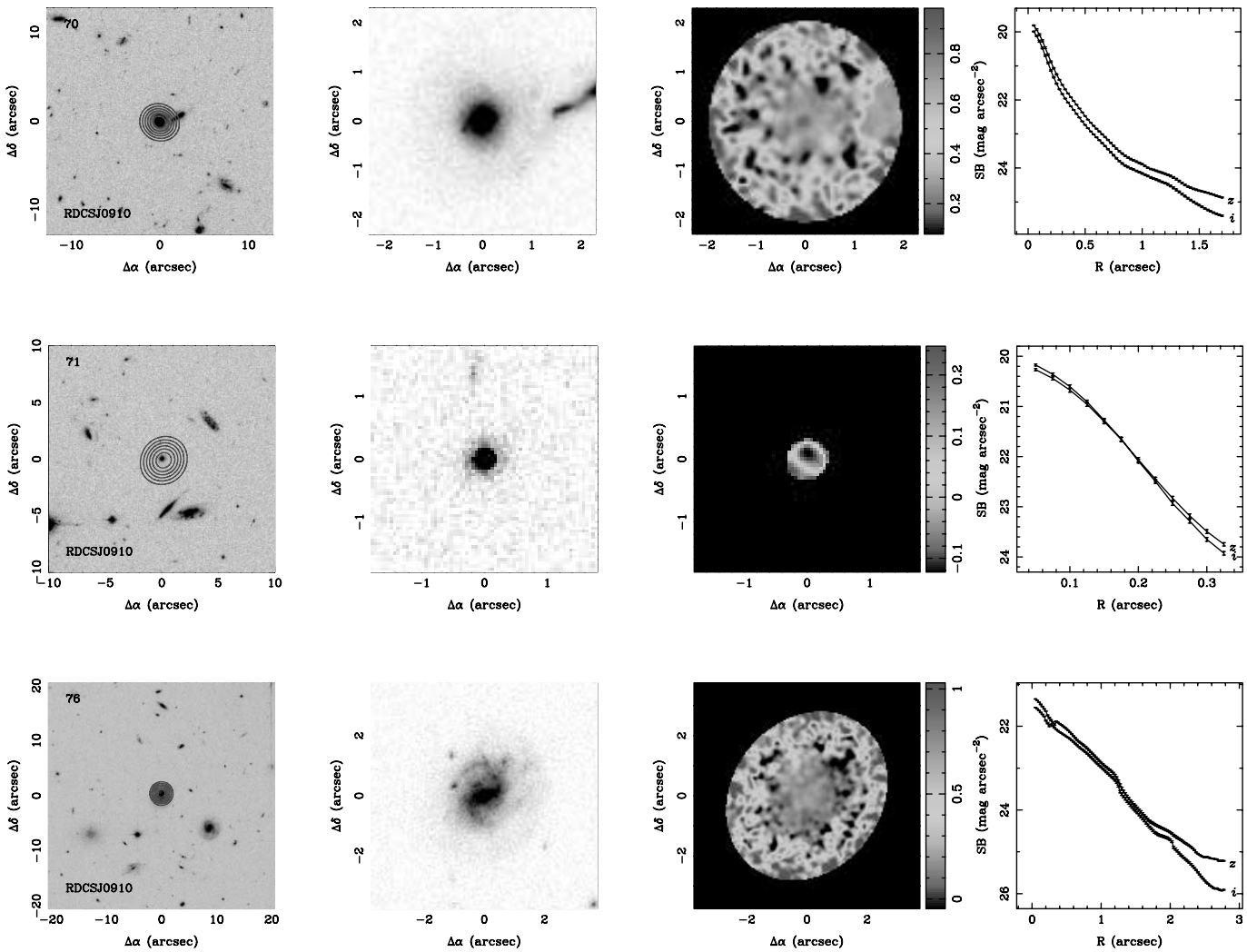

FIG. 3.—*Continued*

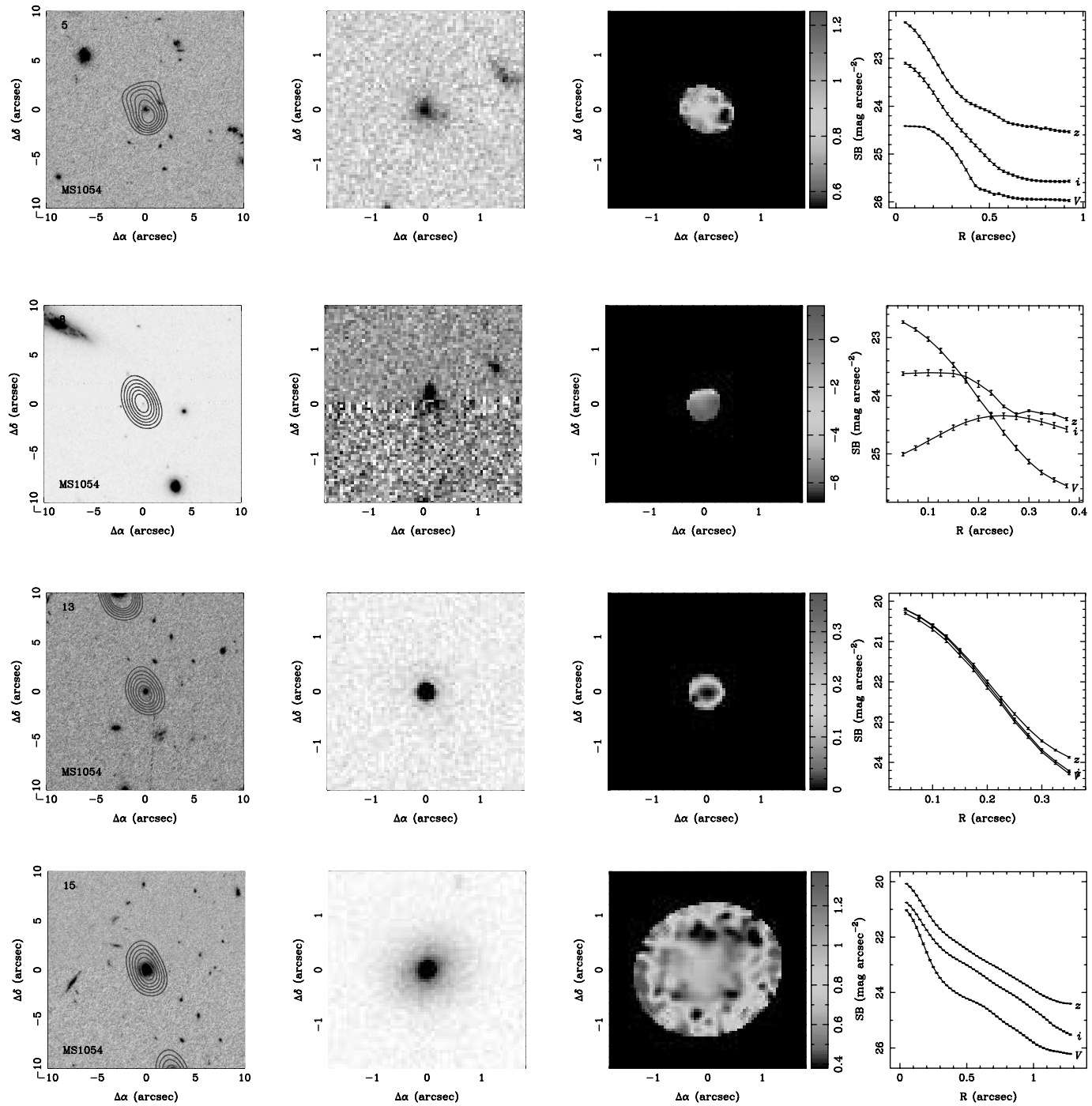

FIG. 4.—Same as Fig. 1, but for MS 1054−0321. [*See the electronic edition of the Supplement for a color version of this figure.*]

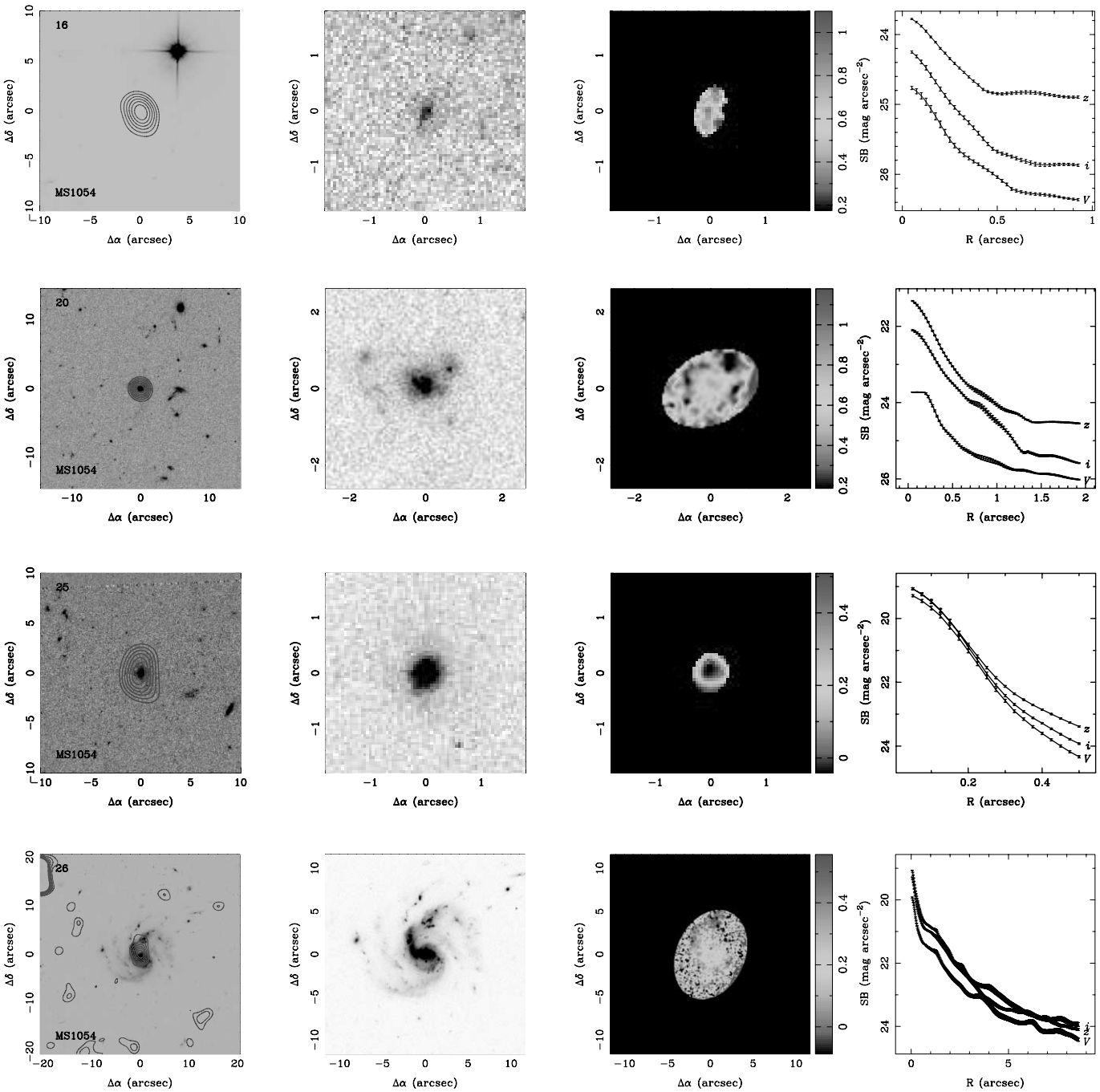

FIG. 4.—*Continued*

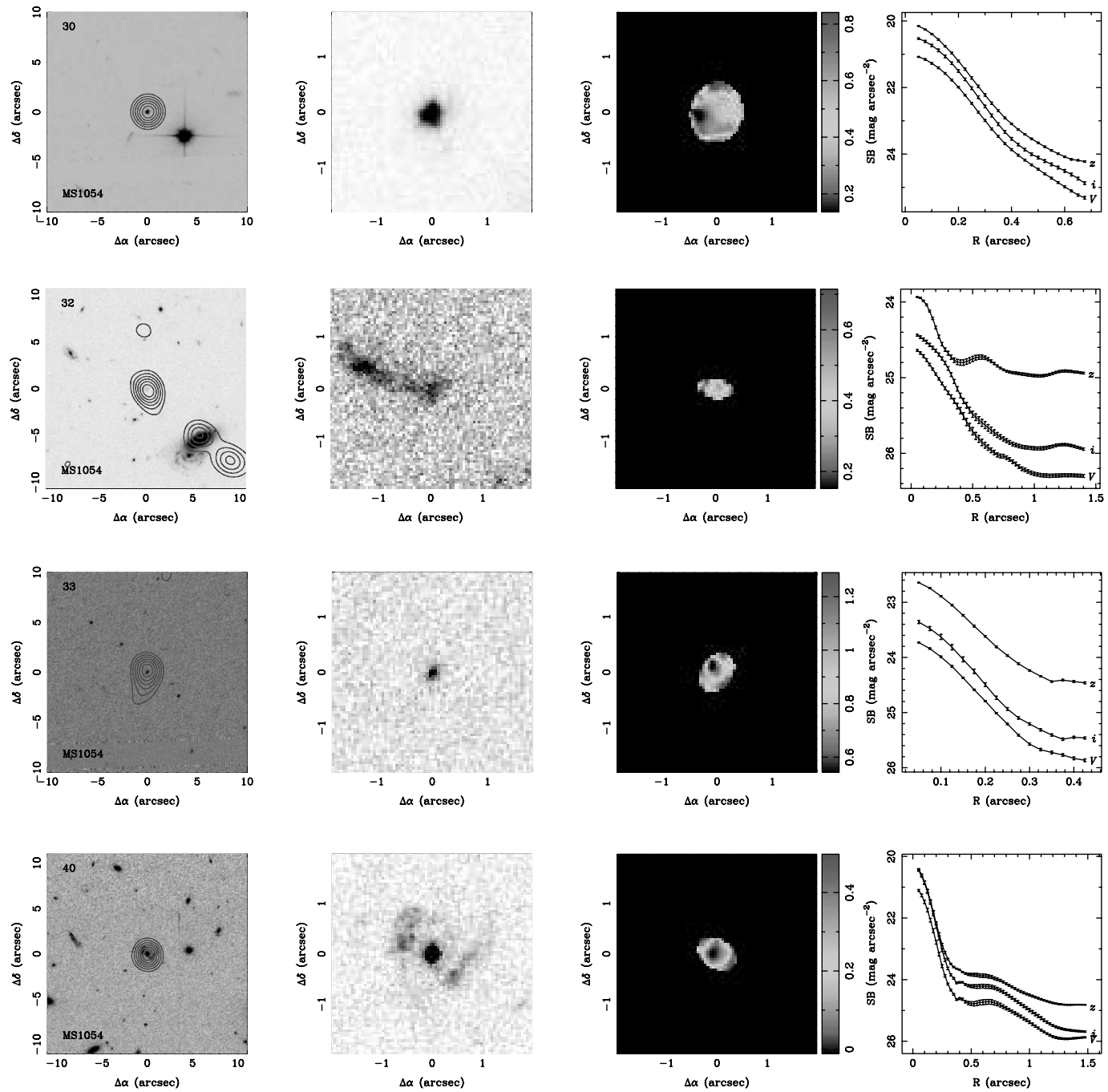

FIG. 4.—*Continued*

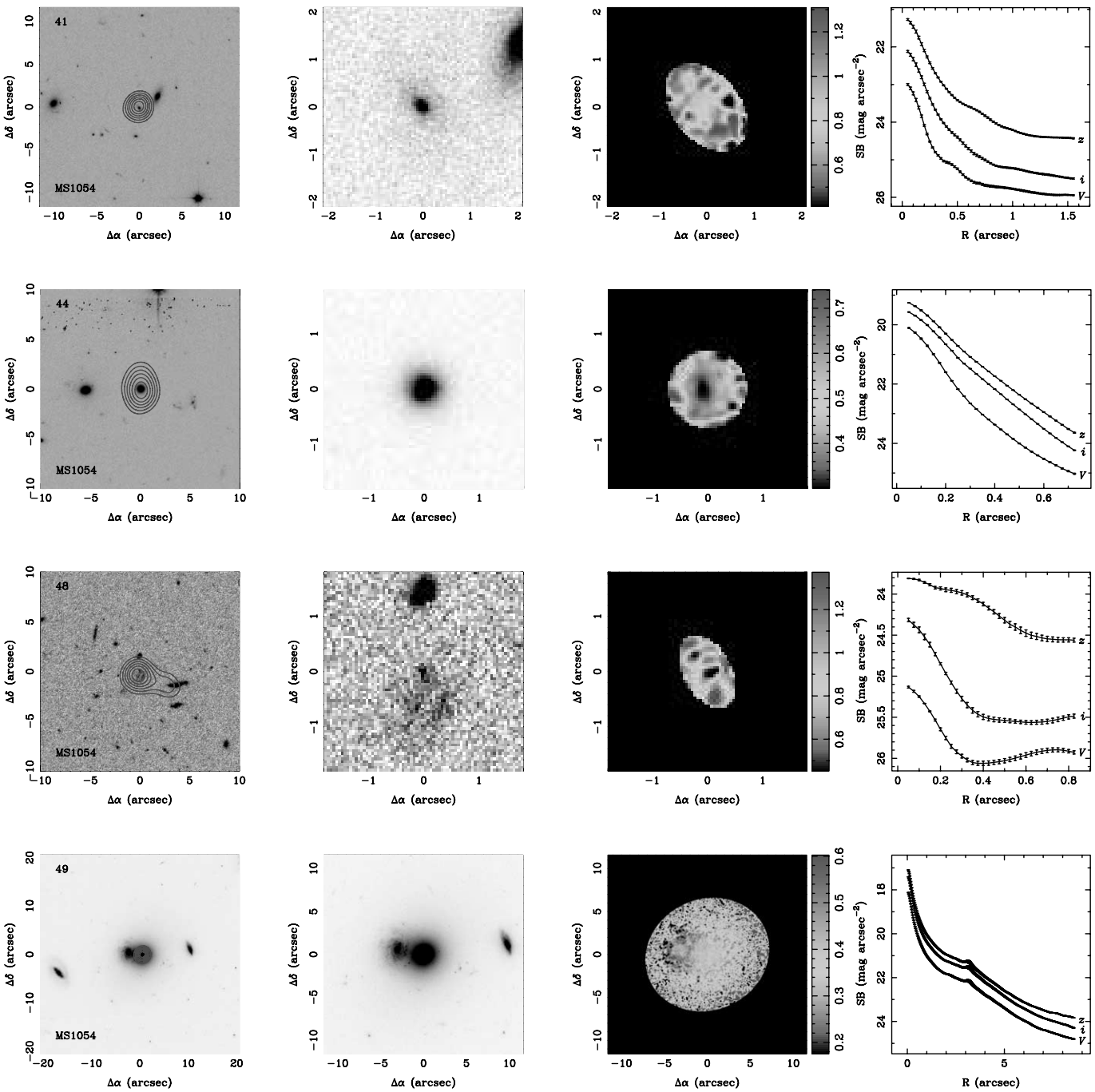

FIG. 4.—*Continued*

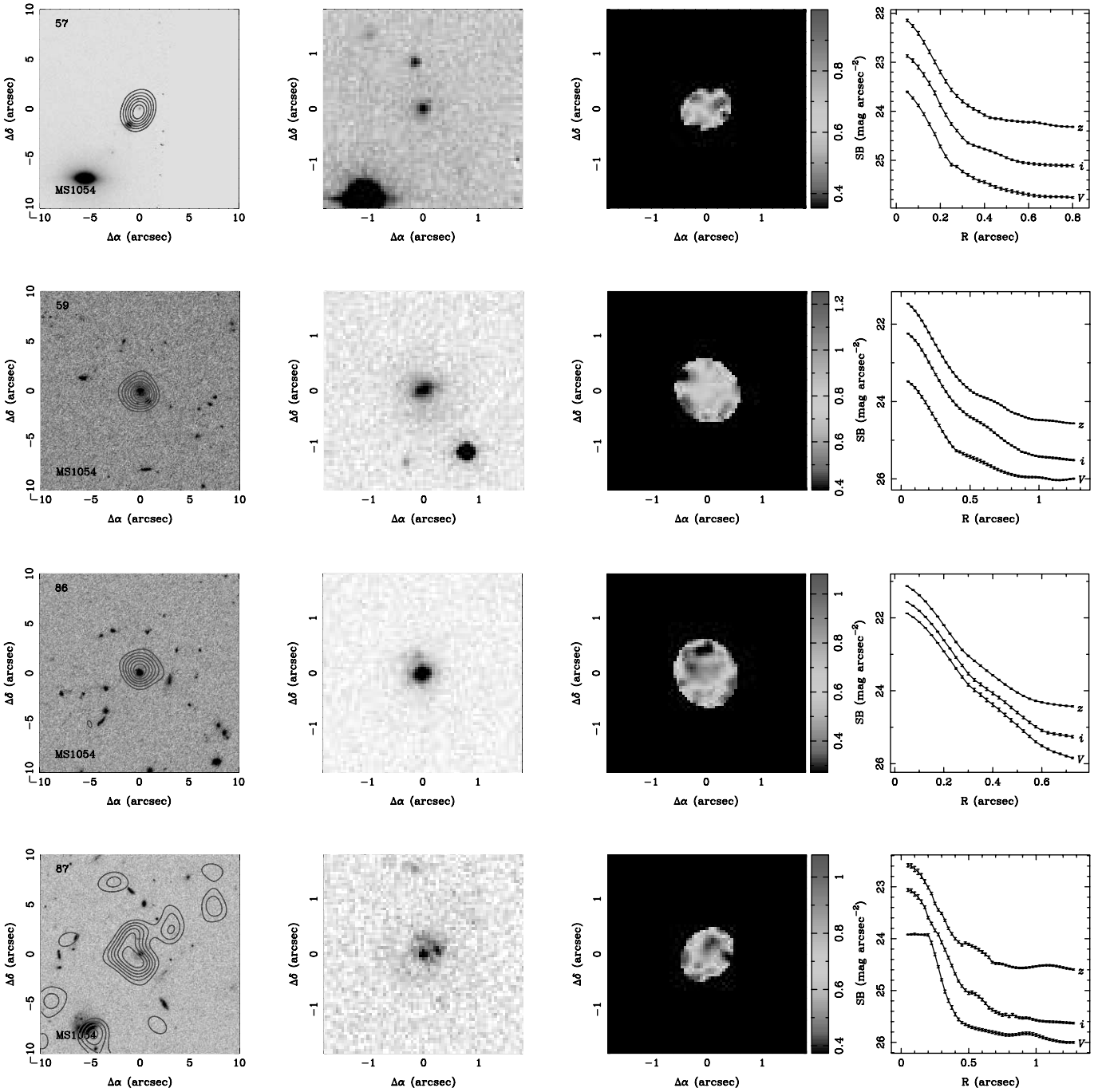

FIG. 4.— *Continued*

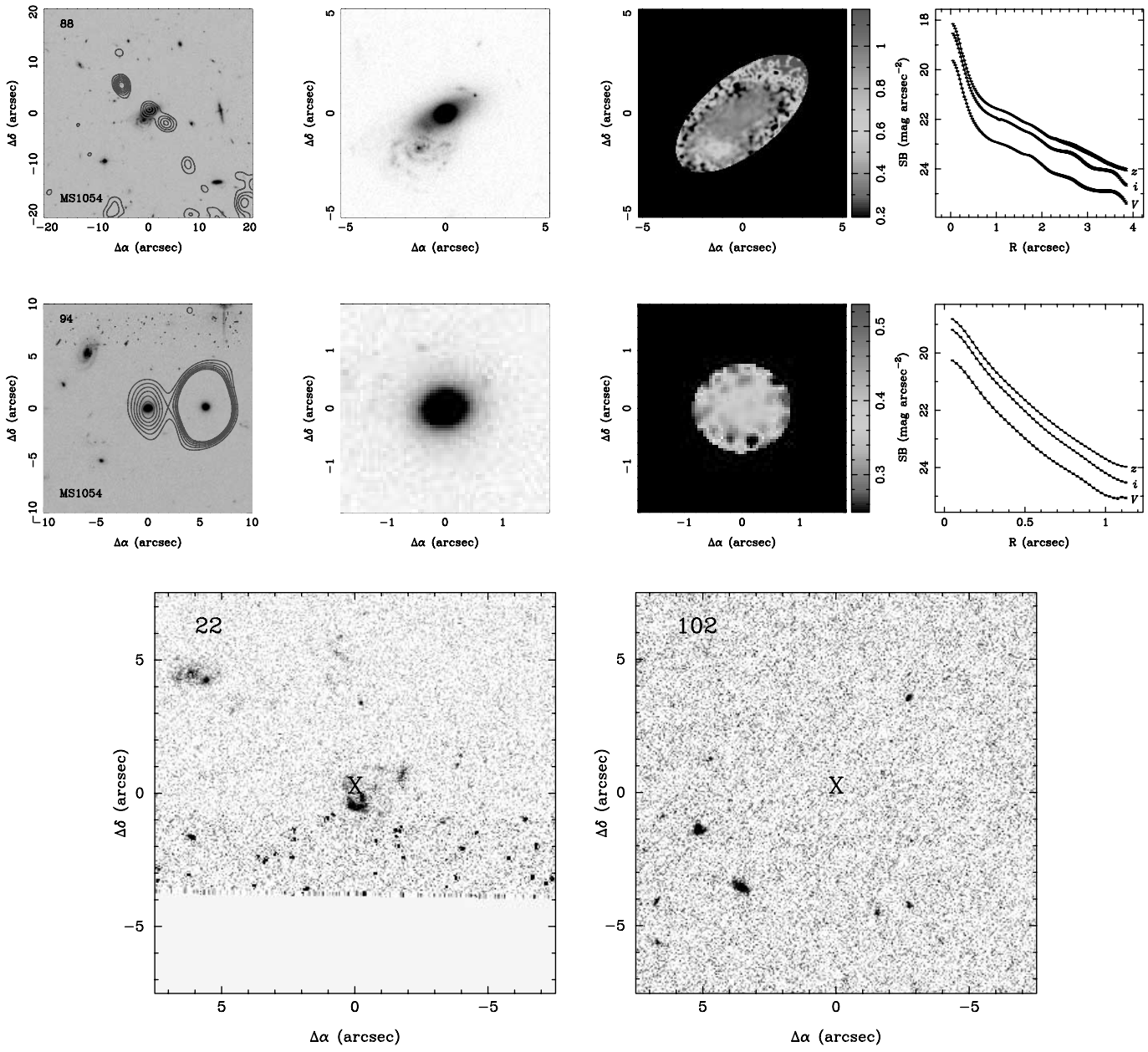

FIG. 4.—*Continued*

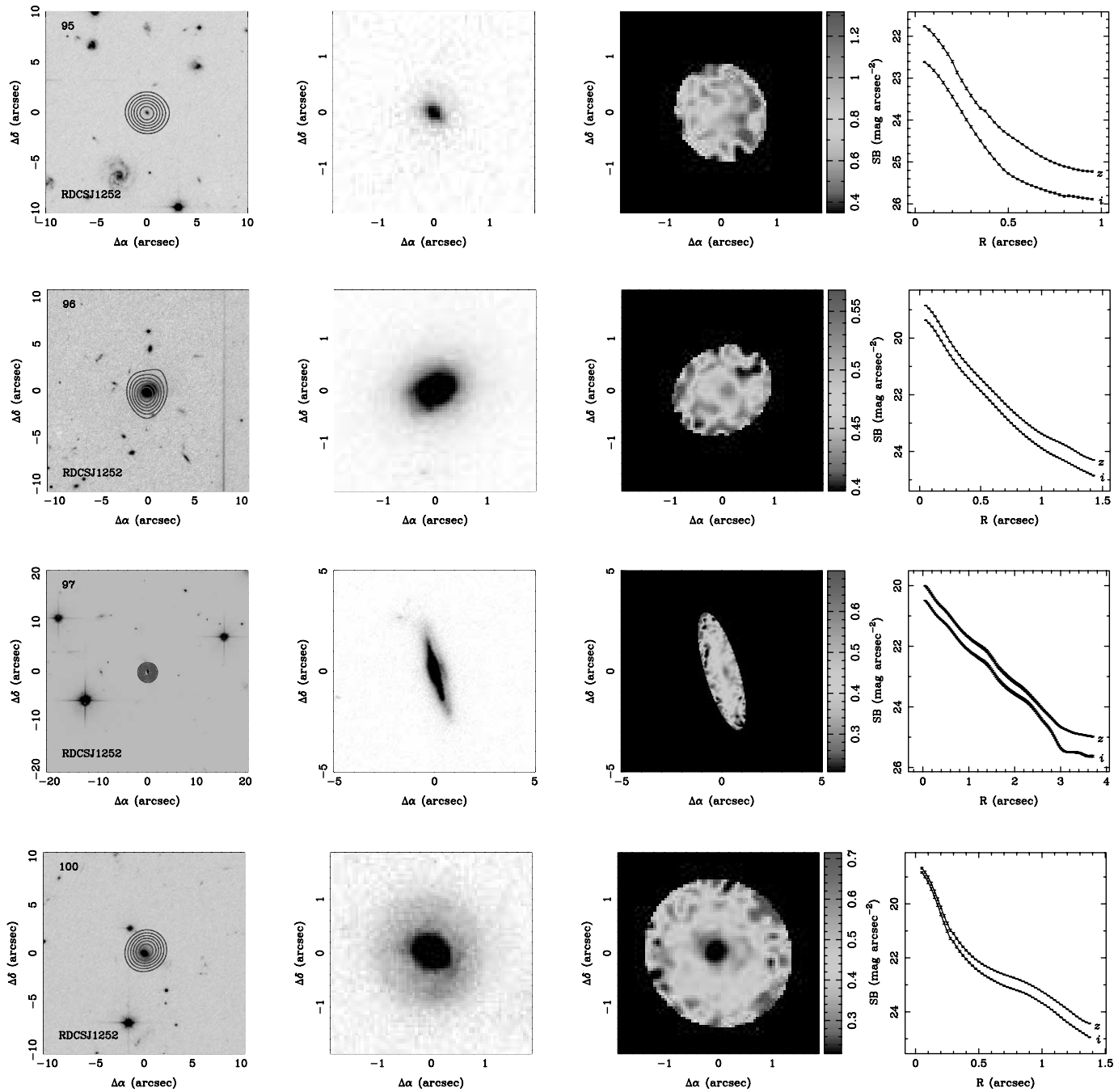

FIG. 5.—Same as Fig. 1, but for RDCS J1252−2927. [*See the electronic edition of the Supplement for a color version of this figure.*]

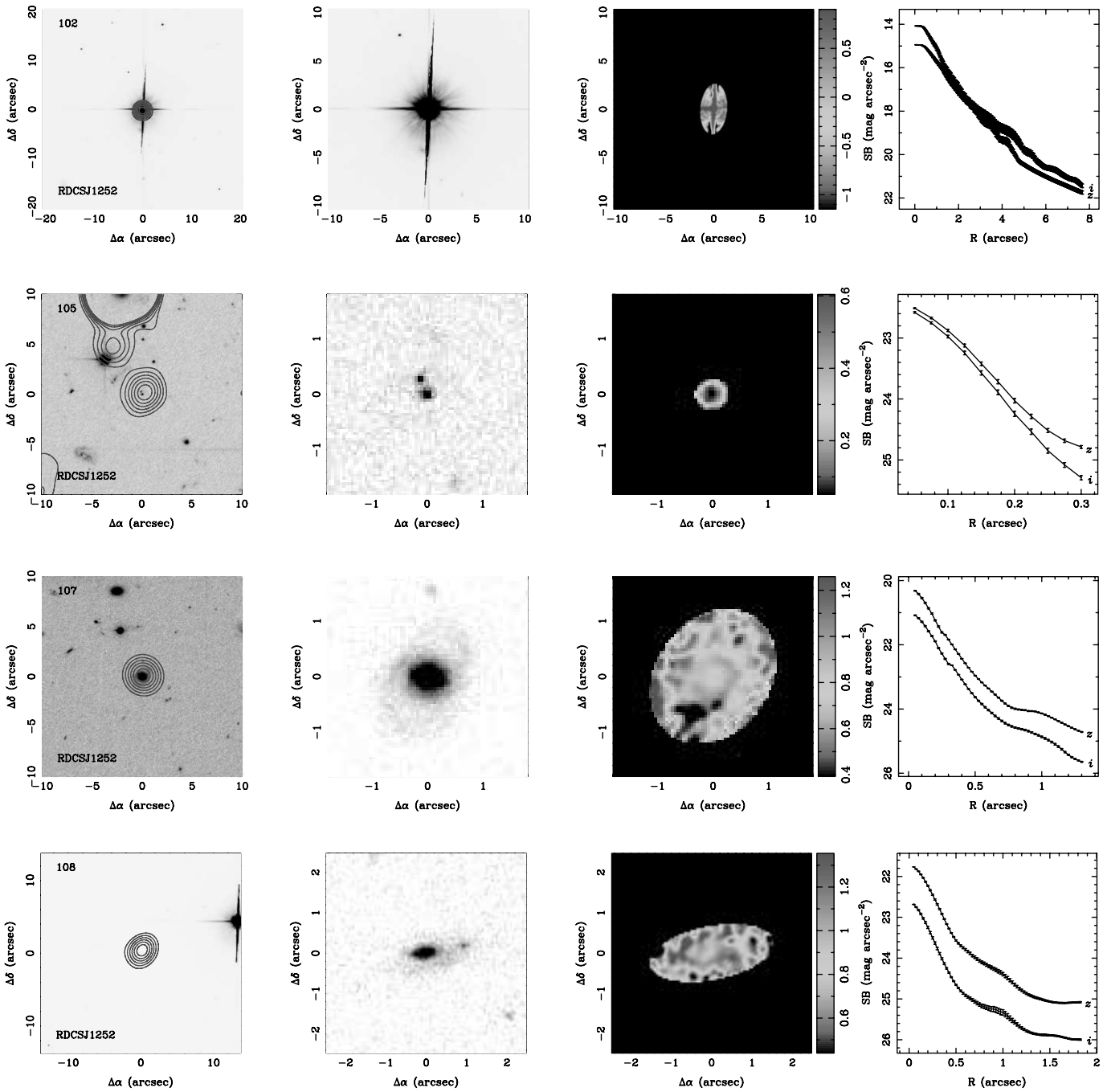

FIG. 5.—*Continued*

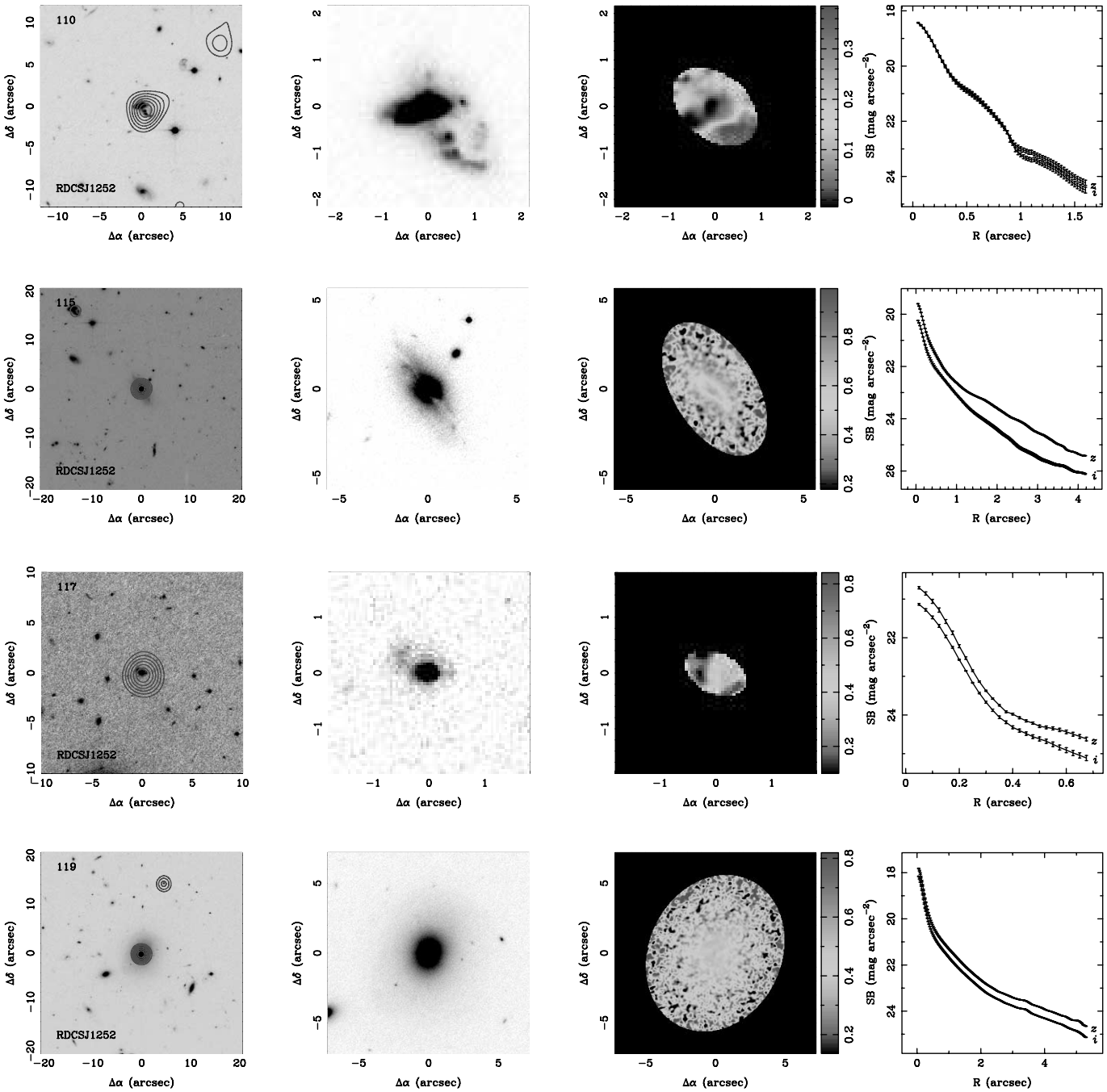

FIG. 5.— *Continued*

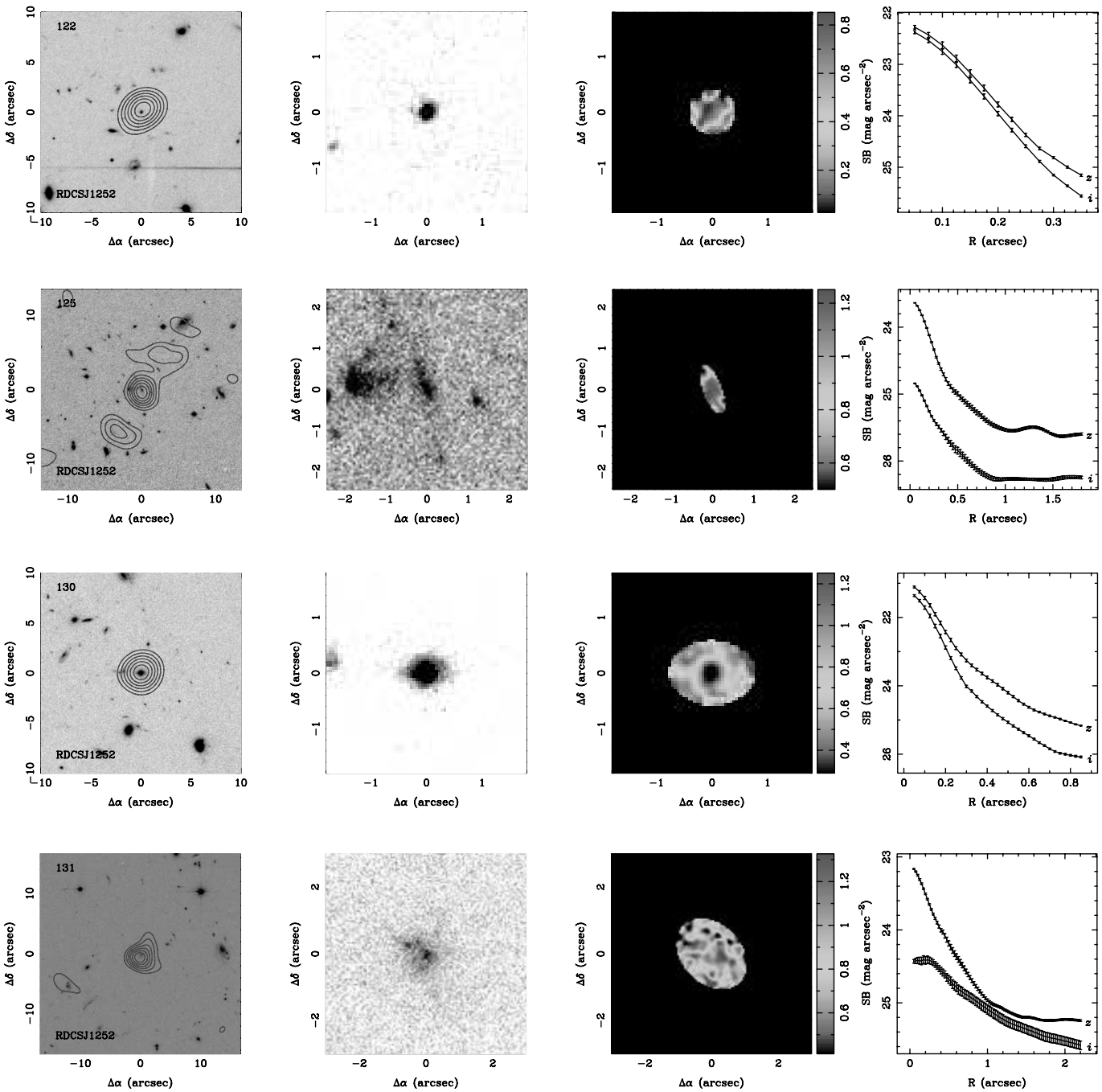

FIG. 5.—*Continued*

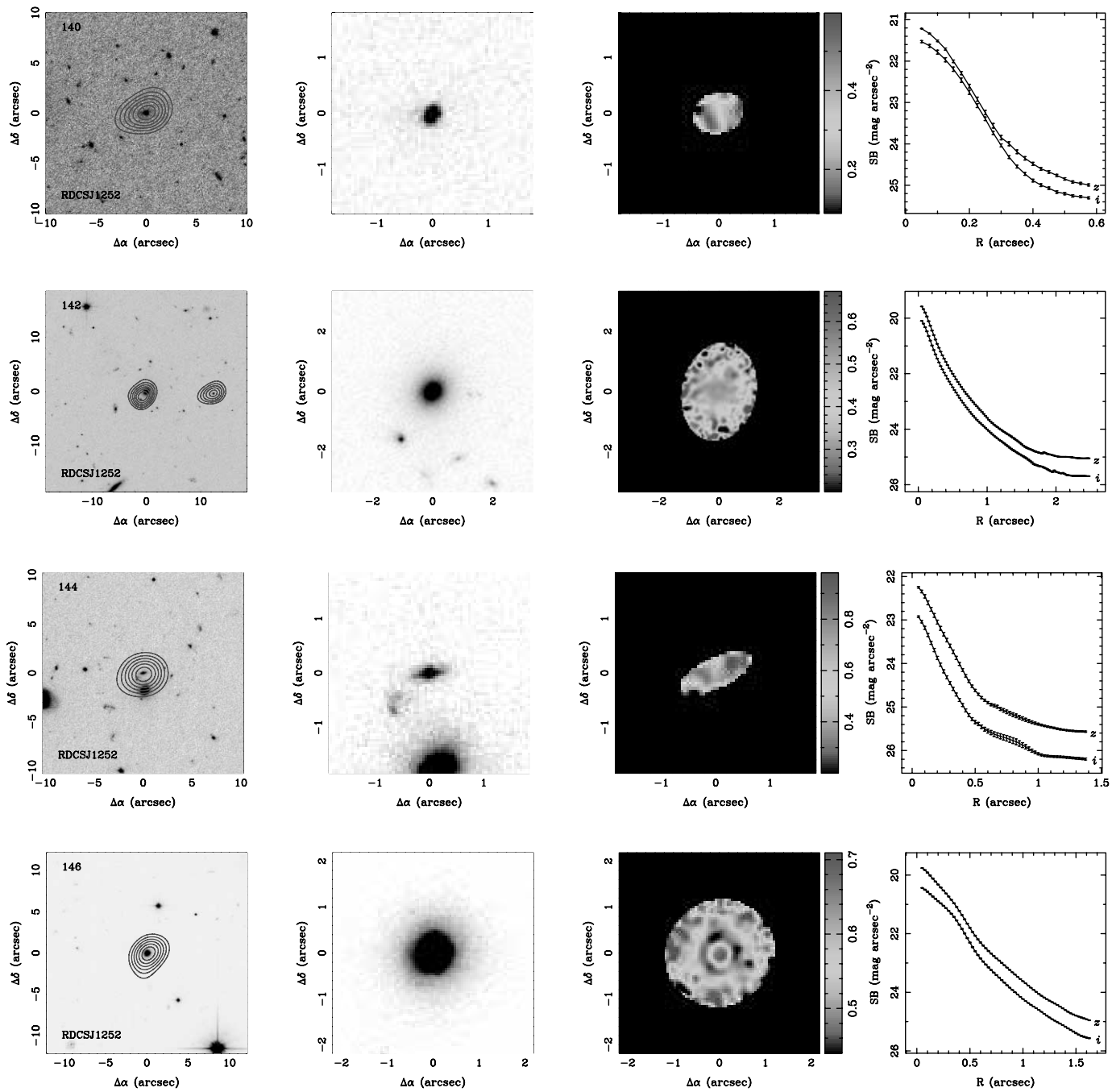

FIG. 5.— *Continued*

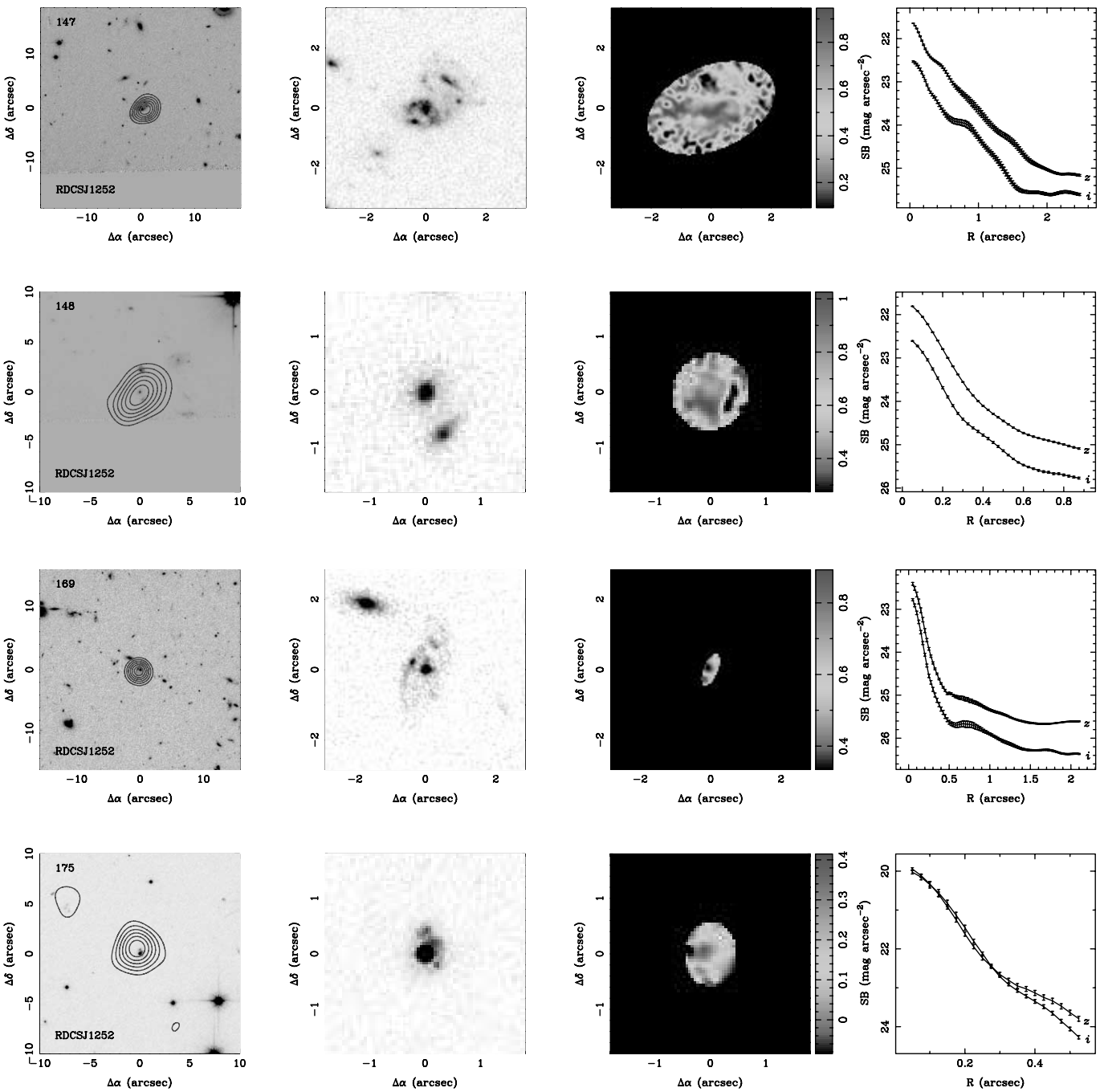

FIG. 5.—*Continued*

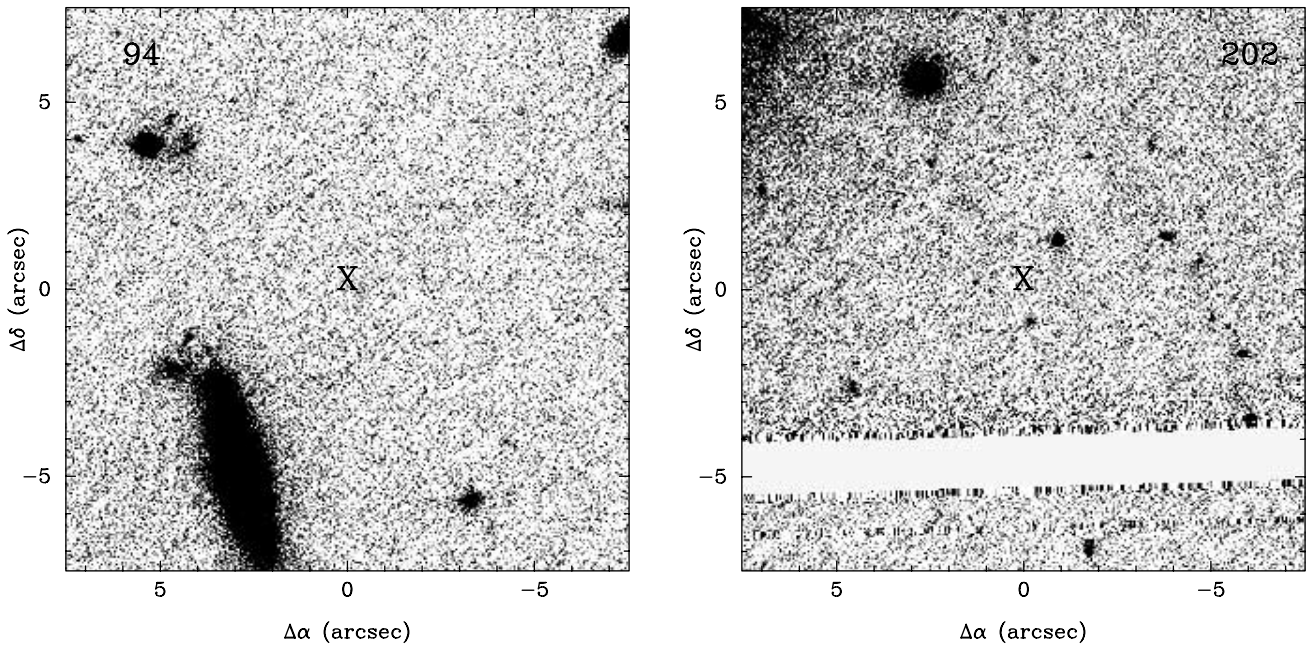

FIG. 5.—*Continued*

gravitational lensing, appear to be less important (Cappi et al. 2001; Johnson et al. 2003).

In Figures 6 and 7, we plot the log N– log S curves over the whole *Chandra* fields for the five clusters for all sources with a S/N ratio >2.1 in their counts and above the flux limits listed in Table 3. This selection yields ∼65 sources in the soft and hard bands of RX J0152, ∼130 for RX J0849, ∼135 for RDCS J0910, ∼80 for MS 1054, and ∼150 for RDCS J1252. The curves are corrected for the sky coverage, which varies as a function of flux. These curves were also derived for the same fields for RX J0849 and MS 1054 by Stern et al. (2002) and Johnson et al. (2003), respectively, but ours make use of an updated X-ray calibration and for MS 1054, a slightly different extraction method. For comparison with a deep field sample, the log N– log S relations of the *Chandra* Deep Field–South (CDF-S; Rosati et al. 2002) and the *Chandra* Deep Field–North (CDF-N; Bauer et al. 2004) are plotted. The relation for the CDF-N is consistent at a 1 σ confidence level with that of the CDF-S (Bauer et al. 2004).

From visual inspection, we immediately find an excess of X-ray sources in the RX J0152, RDCS J0910, and MS 1054 fields over most of their soft and hard fluxes. On the other hand, the curves for RX J0849 are generally consistent with the CDF-S and CDF-N log N–log S relations. The RDCS J1252 field shows an excess at low fluxes ($\lesssim 3 \times 10^{-15}$ ergs s^{-1} cm^{-2}) in the hard band. In terms of source counts in the hard band, we find an excess of a factor of 2.00 ± 0.15 in the number of sources with a flux greater than 2×10^{-14} ergs s^{-1} cm^{-2} in the *Chandra* fields of RX J0152, RDCS J0910, and MS 1054 compared to the CDF-S. On the other hand, for RX J0849 and RDCS J1252, no significant excess is found. Hence, we conclude that the fields of at least three of the five clusters possess a convincing overdensity of X-ray sources.

In Figures 8 and 9, the log N–log S plots are calculated over the smaller ACS mosaics after normalization of the sky coverage. Again, we find an overdensity in the fields of RX J0152, RDCS J0910, and MS 1054. In addition, in the hard band, the RX J0849 and RDCS J1252 data show an excess at fluxes of $\lesssim 6 \times 10^{-15}$ ergs s^{-1} cm^{-2}. There also appears to be a deficit of sources in RDCS J1252 at $\approx 2 \times 10^{-15}$ ergs s^{-1} cm^{-2} in the soft band. These results therefore strongly suggest that the overdensities of X-ray point sources are directly associated with the cluster structures.

3.2. *The Host Galaxies*

As seen in Figures 1–5, the morphology of the optical counterparts varies considerably, from compact and core-dominated to elongated and diffuse. To parameterize the morphology more objectively than visual estimations, we plot the asymmetry (A) and central concentration (C) indices of the resolved optical candidates with $i_{775} \leq 25.5$ in Figure 10, using the public software package PyCA developed by one of us (Menanteau et al. 2004, 2006). The sources are labeled by their X-ray class, when available. The three morphological groups are demarcated into regions derived from one of the parallel UDF fields (Menanteau et al. 2006), which is representative of a field sample. In this automatic classification scheme, we find that ∼52% of the counterparts are early types, ∼35% are late types and the remainder are irregulars. Among the common, albeit limited, sample of AGN-1 and AGN-2 X-ray classes, ∼48% are located in the early-type category, ∼42% in the late-type category, and the remainder in the irregular category.

The optical identifications also include some faint ($i_{775} \approx 25.5$–28) and amorphous nebulosities with no obvious nuclei and with very low and uniform surface brightnesses (∼24–26 mag arcsec^{-2} in i_{775}), near the detection threshold of the ACS images. These roughly represent ∼10% of the sample. Some examples include ID 60 in RX J0152, IDs 58, 93, 102, and 104 in RX J0849, ID 40 in RDCS J0910 and IDs 16, 32, and 48 in MS 1054. These sources are detected in all the ACS bandpasses of a given cluster and so are unlikely to be bona fide *i*- or *z*-band dropouts. Deeper imaging would help characterize the structure and photometry of these candidates.

We find no convincing cases of non detections of optical counterparts at the location of any bright X-ray source, although in some cases, such determinations may be compounded by source confusion in these crowded fields or by very faint nebulosities.

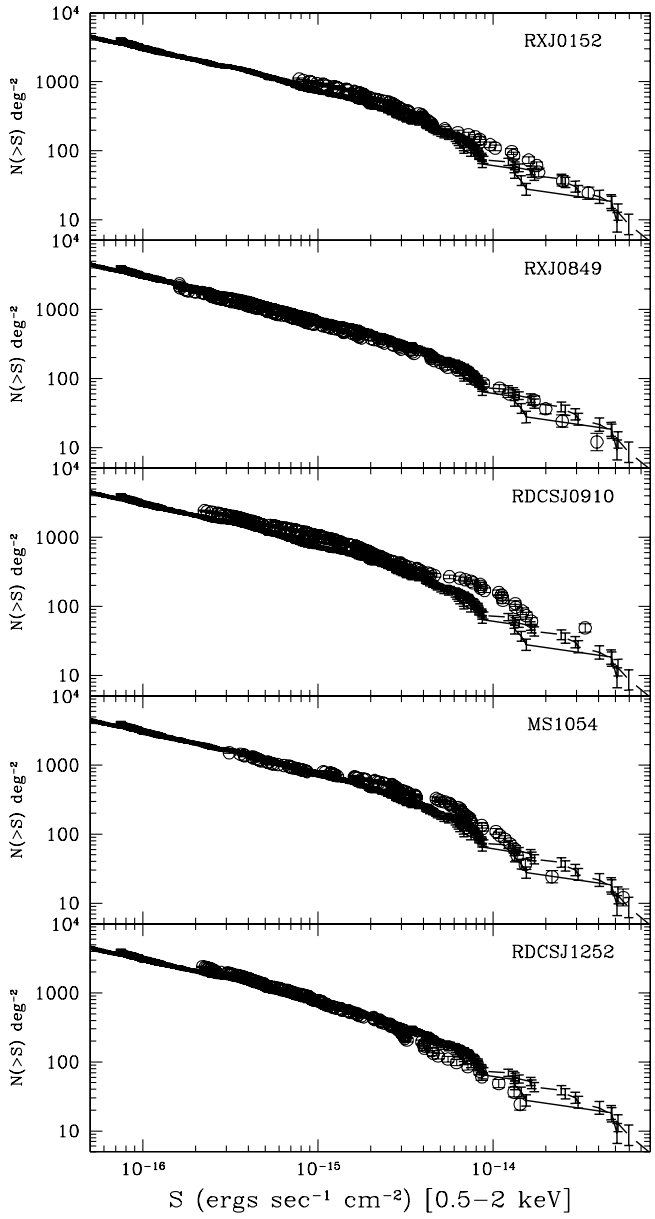

FIG. 6.—Soft band $\log N(>S) - \log S$ relations for the five clusters are plotted as open circles over the *Chandra* fields. For comparison, the CDF-S relation from Rosati et al. (2002) is shown as a solid line and the CDF-N relation from Bauer et al. (2004) as a dashed line. Poissonian errors are assumed on the counts.

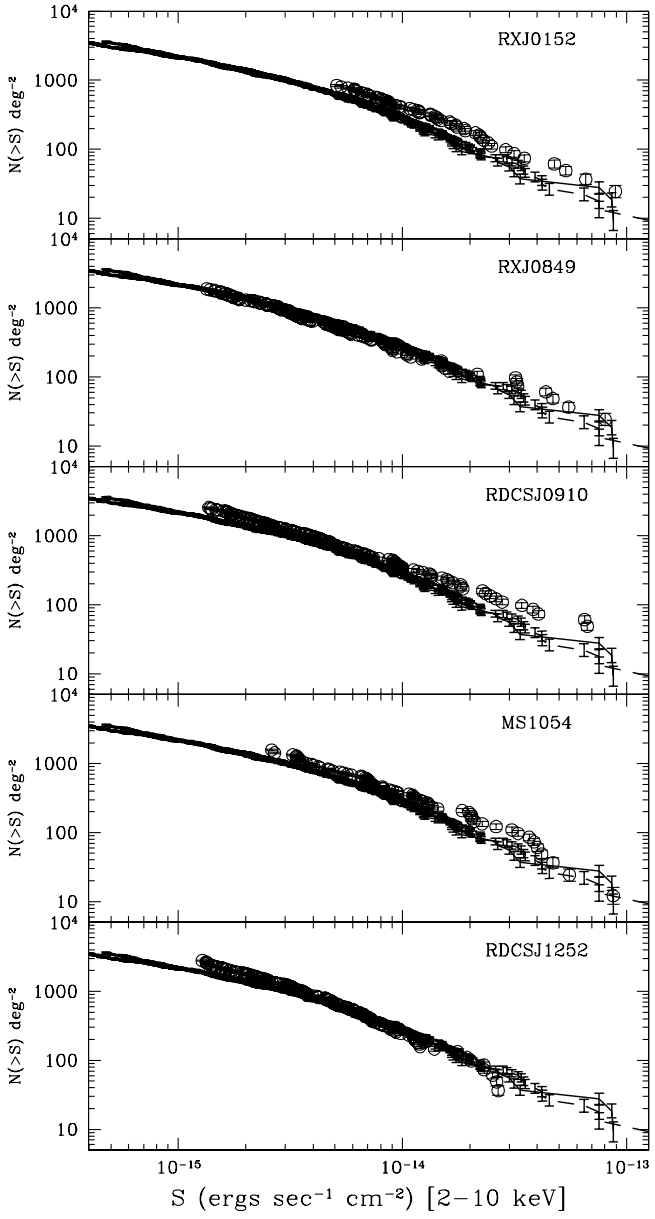

FIG. 7.—Same as Fig. 6, but for the hard band.

Two possible candidates are ID 102 in MS 1054 and ID 94 in RX J1252, but their X-ray fluxes are suspiciously close to the detection thresholds.

Such blank optical fields have been found, for example, in the ACS fields of the Great Observatories Origins Deep Survey (GOODS; Koekemoer et al. 2004; Giavalisco et al. 2004) and in the Multiwavelength Survey by Yale-Chile (MUSYC; Urry et al. 2005). Infrared counterparts to some of the GOODS sources are detected with *Spitzer*, and fits to their spectral energy distributions are generally consistent with evolved, dust-free populations at large redshifts ($z \sim 2$–5) or with dusty reddened star-forming populations, except possibly for one object, which may possess a higher redshift (Koekemoer et al. 2005). The depths of our cluster images of RX J0849, RDCS J0910, and RX J1252 are comparable to those of the GOODS field in the common filters i_{775} and z_{850} and significantly deeper in the cores where the different pointings overlap, while the fields of RX J0152 and MS 1054 are slightly shallower than GOODS. Hence, our success rate in associating optical and X-ray sources should be roughly similar, if not better, to that of the GOODS work.

3.3. *The Nuclei*

Several of the X-ray–selected galaxies possess an unresolved nucleus, a common signature of nuclear activity at visible wavelengths (e.g., Jarvis & MacAlpine 1998). From visual examination, we find that ~40% of our optical identifications possess an unresolved nucleus. The majority (~53%) of these nuclei are imbedded in late-type host galaxies, while the rest are found in early types (~40%) and irregulars. Among the late types, a majority (~90%) exhibit roughly face-on spiral structure, suggesting that obscuration by dust in the plane of the galaxy masks out weaker nuclei in more edge-on systems and thus may lead to underestimates in their number counts. We note that our visual selection is biased against point nuclei in early-type galaxies because of the possibly poor contrast between a weak point source and its underlying, steep de Vaucouleurs light profile.

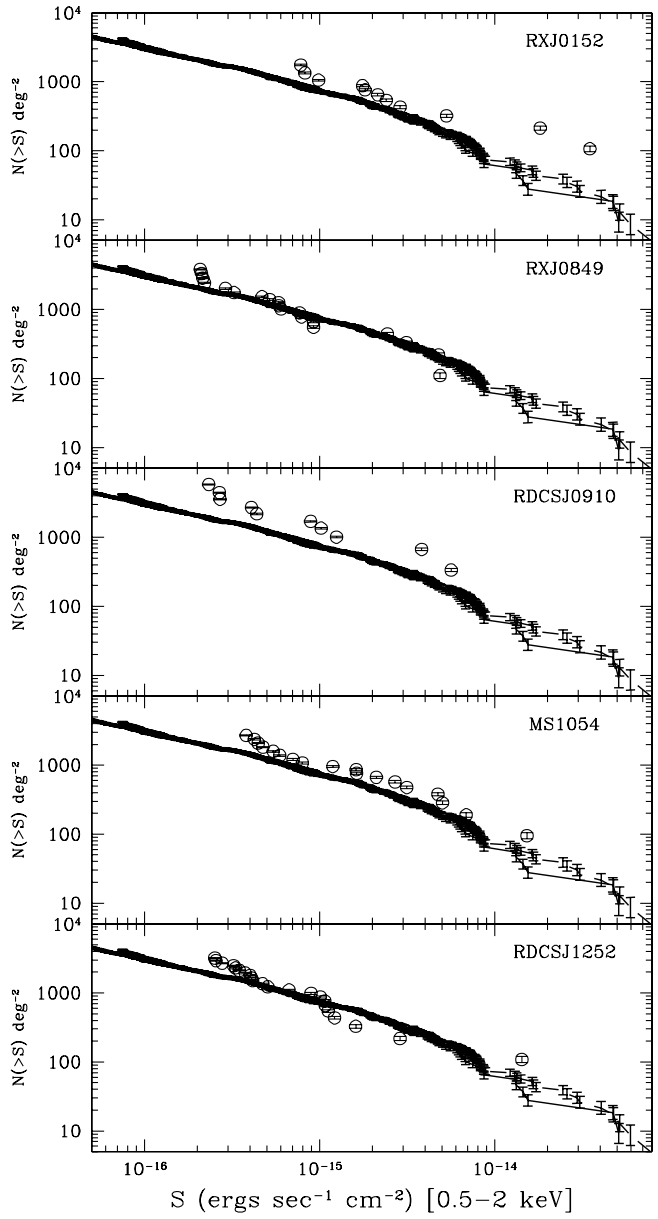

FIG. 8.—Same as Fig. 6, but over the ACS mosaics only.

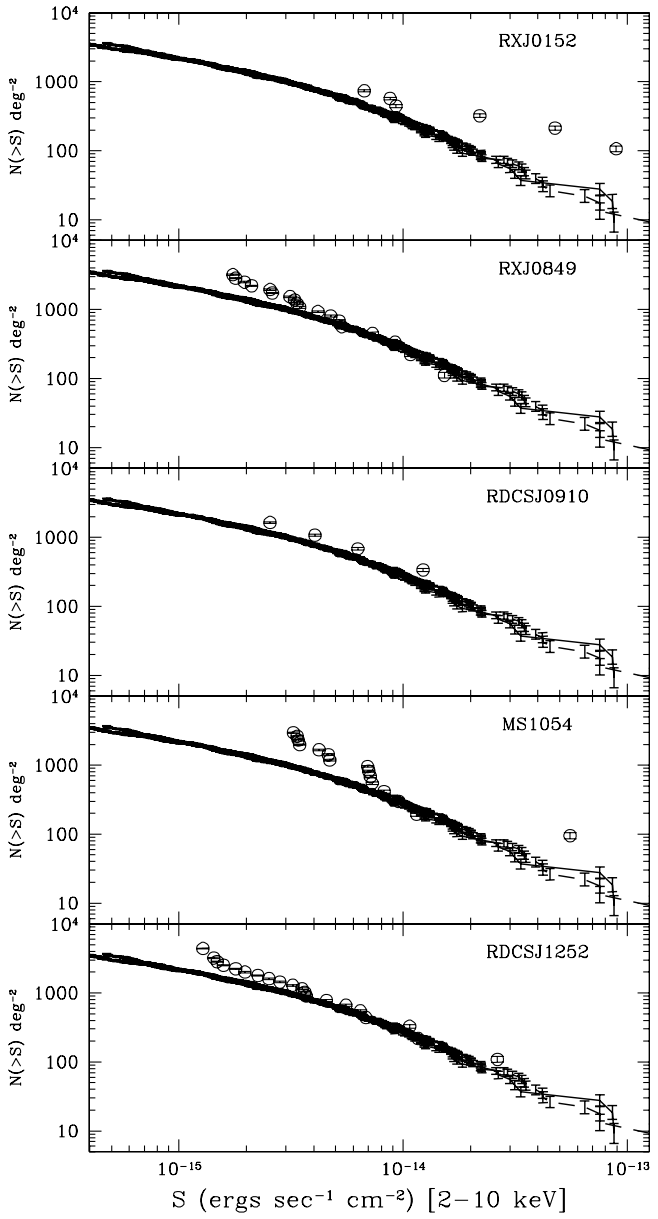

FIG. 9.—Same as Fig. 7, but over the ACS mosaics only.

In Figure 11, the X-ray (F_X) and optical ($F_{i,\mathrm{gal}}$ and $F_{i,\mathrm{nuc}}$) fluxes and magnitudes of the galaxies and their nuclei, as well as their ratios, are compared. We consider the hard X-ray flux, which we assume to originate in the spatially unresolved nucleus. In the left panels, the relations are shown with respect to the integrated flux and magnitude of the galaxies, while in the right panels, they are compared to the nuclear flux and magnitude. The nuclear magnitudes were extracted in an aperture with a radius of 3 pixels with the PyRAF `phot` task and corrected for the underlying galaxy by calculating the background in an annulus between 4 and 6 pixels. As above, only galaxies (and their nuclei) with magnitudes of $i_{775,\mathrm{gal}} \leq 25.5$ are considered.

From the bottom panels of Figure 11, there is a clear trend for the fainter galaxies and nuclei to possess higher X-ray to optical flux ratios, F_X/F_i. This correlation holds for both the galaxy's integrated light and for the nuclei alone, consistent with a nuclear origin for the hard X-ray flux.

The simplest interpretation for this trend is an increase in obscuration toward the nuclei, which would result in lower optical magnitudes and hence, in an enhancement in the X-ray to optical flux ratios. To verify whether F_X/F_i is in fact sensitive to obscuration by dust, we plot this quantity in Figure 12 as a function of galaxy inclination, $\cos^{-1}(1-e)$, where e is the ellipticity calculated by SExtractor. In the top panel, we find that $F_X/F_{i,\mathrm{nuc}}$ for the late types correlates with inclination angle. This is confirmed by the Spearman rank-order correlation coefficient $r_s = 0.44$ and its high significance of $p = 0.02$. The sense of the correlation is as expected: the more edge-on late types (large inclinations), and thus those with the most obscured nuclei, have the highest $F_X/F_{i,\mathrm{nuc}}$. No correlation is found for the early types (*middle panel*), as expected. In the bottom panel, we also find no correlation between $F_X/F_{i,\mathrm{gal}}$ and the inclination angle for either the early- or late-type galaxies. This indicates that the outer parts of the galaxies suffer little extinction, at least compared to the nuclei, and is also consistent with a nuclear origin for the X-ray emission.

The above analysis assumes that the X-ray to optical flux ratios are not too sensitive to the shifting of the galaxies spectral

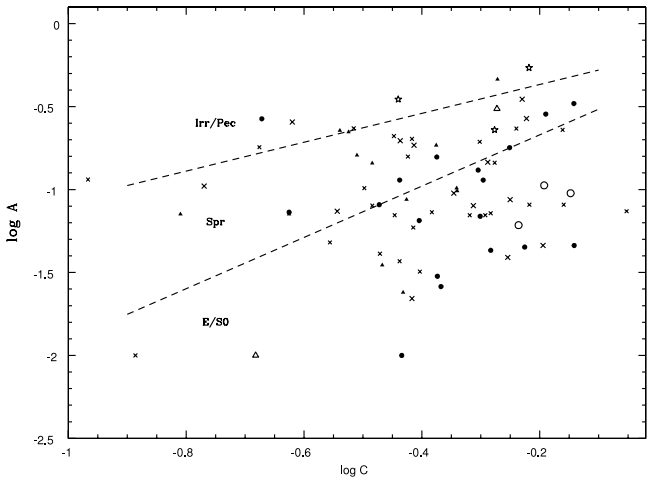

FIG. 10.—Asymmetry (A) and central concentration (C) indices are plotted for the optical counterparts to the *Chandra* sources. The symbols are (*filled circles*) AGN 1; (*filled triangles*) AGN 2; (*open circles*) QSO 1; (*open triangles*) QSO 2; (*star*) galaxy; (*crosses*) all others with no X-ray class. The dashed lines separate the three morphological classes and are derived from one of the UDF parallel fields (Menanteau et al. 2006).

energy distributions due to the redshift i.e., the K-band correction. We can crudely test for this effect by limiting the sample of late-type galaxies to a narrow range of redshifts. Because of the paucity of reliable redshifts and the need for reliable statistics, we choose a range of $z = 0.8$–1.5, which has the added benefit of spanning the redshift interval of the five clusters. We then find a slightly stronger correlation between $F_X/F_{i,\mathrm{nuc}}$ and the inclination ($r_s = 0.66$ and $p = 0.01$). Disentangling evolutionary and intrinsic effects will be possible when accurate redshifts become available for a larger number of sources in this study.

3.4. *Color Inhomogeneities in the Early-Type Galaxies*

The existence of field early types with blue central regions at intermediate redshifts ($0.4 \lesssim z \lesssim 1.0$) and internal color variations that depart from the expectation for passively evolved ellipticals has been known for some time (e.g., Menanteau et al. 2001a, 2004). In most cases, the color variations manifest themselves via the presence of blue cores, an effect opposite in sign to that expected from metallicity gradients in passively evolved ellipticals. However, the exact physical nature of these objects has been elusive. Before the advent of ACS, they had been detected only in extremely deep broadband *HST* WFPC2 observations (e.g., the HDFs) and deep spectroscopic observations have been rather limited due to the long integration times required to acquire a high-signal spectrum.

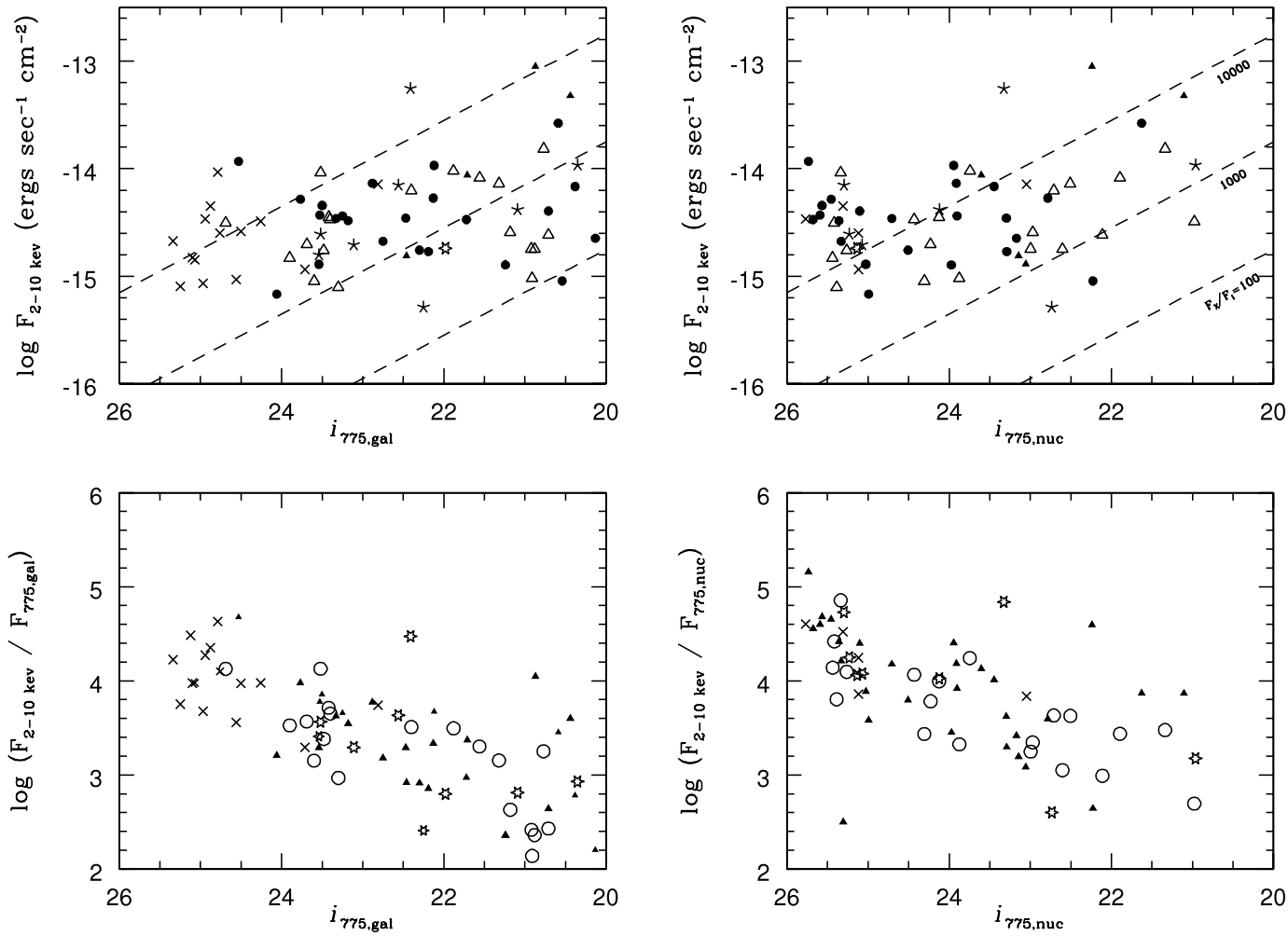

FIG. 11.—In the left panels, the hard X-ray flux and its ratio with respect to the integrated galaxy flux in the i bandpass are plotted with respect to the galaxy i_{775} magnitude. In the right panels, the same quantities are plotted but with respect to the galaxy nuclear magnitude. The symbols are (*open circles*) early types; (*filled triangles*) late types; (*stars*) irregulars; (*crosses*) no visual classification.

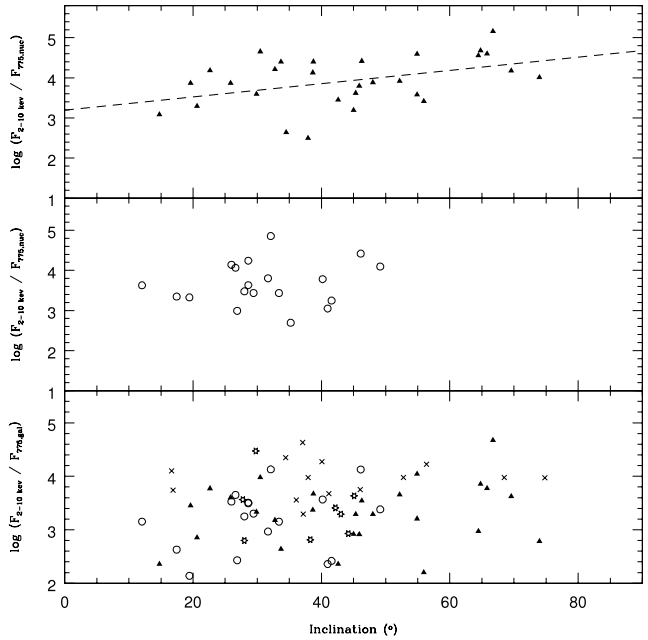

FIG. 12.—Hard X-ray to optical flux ratios are plotted as a function of the galaxy inclination angle for the nuclei of the late types (*top*) and the early types (*middle*) as well as for the integrated galaxy (*bottom*). The symbols are as in Fig. 9. The dashed line is a linear fit to the $F_X/F_{i,\mathrm{nuc}}$ data points of the late types.

Blue cores in early types have traditionally been associated with star formation attributed to differences in the local potential well in the galaxies' central regions (Menanteau et al. 2001b; Friaça & Terlevich 2001). But recently, some blue core early types have been associated with luminous X-ray sources, suggesting that at least in these objects, the nonthermal emission from the central AGN may contribute significantly to the observed central color gradients (Menanteau et al. 2005a, 2005b; Treu et al. 2005). But the complete picture is more complicated: the spectra of some of these galaxies show the unambiguous signatures of both AGN activity *and* star formation. It is then quite natural to relate the galaxy's central blue light with the rapid mass infall into a central supermassive black hole, a process that might trigger circumnuclear star formation. Hence, these blue-nucleated early-type galaxies may represent an excellent laboratory for exploring the AGN-starburst connection at $z \approx 1$.

Some early-type galaxies at intermediate redshifts also possess off-nuclear blue clumps. These have been identified, for example, in the Ultra Deep Field (Elmegreen et al. 2005; Pasquali et al. 2006) and have been interpreted as young star-forming regions. The origin of the gas that produces these blue inhomogeneities is unknown. Both an internal and external origin have been postulated. The clumps may be tidally induced starbursts in already existing gas triggered by interaction with a nearby galaxy. On the other hand, the clumps could be the remnants of an externally accreted small galaxy. Because of their young age, the blue stars would have formed after entering the spheroid (Elmegreen et al. 2005). Curiously, the early types do not exhibit the classical signatures of merger events such as tidal tails and isophotal distortions, suggesting that in this scenario, they are very late stage mergers.

Do the early types in our AGN sample possess blue cores? An examination of the $i - z$ color maps (Figs. 1–5) of all the galaxies that we visually classified as early types reveals that ~50% of the AGN hosts possess a "classical" blue core, characterized by a smooth blue halo centered on the nucleus. Although no definite census is yet available, the frequency of blue core early types is thought to be ~10% of the general population of intermediate-z early types. Hence, the detection of blue cores in approximately half of our sample is significant and indicates a strong association with AGN activity.

Nondetections of blue cores may be due to an intrinsically weak AGN and/or to our use of a single color. Although convenient because it is common to all five clusters, the $i - z$ color in fact probes different parts of the galaxies' SEDs because of the different redshifts (typically $z = 0.6$–1.3) and so may not be the ideal color discriminant. The best contrast in $i - z$ between a blue core and a red host is for $z \approx 1.1$, where the contribution from the old stellar population of the galaxy decreases sharply in i_{775} blueward of the 4000 Å break, while the AGN and/or starburst contribution increases rapidly. Hence, a more rigorous identification of blue cores requires the use of multiple colors.

A remarkable early-type galaxy in our sample is ID 146 in the field of RDCS J1252. At $z = 0.844$, it is located in the foreground of the cluster and is classified as an AGN-1 from its X-ray luminosity. Its $i - z$ color map shows a beautiful, symmetric blue ring of diameter ≈5 kpc (0.7″) centered on the nucleus. Our tests show that the ring is not an artifact of the PSF matching when assembling the frames into color maps. Moreover, there are clear differences in the structure and flux of the galaxy at the location of the ring between the i_{775} and z_{850} images. Such a ring is reminiscent of circumnuclear star-forming rings usually associated with barred spirals and forming near resonances under the influence of gravitational torques from the bar. They are the sites of young (≲100 Myr) super star clusters and are typically a few hundred parsecs in size (e.g., Maoz et al. 1996). The asymmetry and concentration indices of ID 146 place it firmly in the domain of early types. Hence, the presence of a ring in this galaxy, possibly the site of vigorous star formation, is highly unusual. We note that there are no obvious signs of interaction with other galaxies: the outer isophotes of the galaxy are smooth and regular and, except for a few faint nebulous patches, there is no other galaxy in its immediate vicinity (≲5″).

3.5. *The Local Environment*

Do the galaxies hosting the AGNs possess an excess of companions compared to normal galaxies in the same fields? Although past studies have sometimes produced ambiguous results, primarily because of the varying selection criteria of the AGN and control samples, such as morphology and luminosity, the general consensus appears to be that galaxies with active nuclei are more likely to be part of close pairs, possibly inducing nuclear activity through tidal perturbations. At low redshifts, the results have been mixed for Seyfert galaxies (Dahari 1985; Fuentes-Williams & Stocke 1988; Virani et al. 2000). On the other hand, more luminous quasars are usually found in small groups of galaxies, possibly increasing in richness at higher redshifts (e.g., Bahcall et al. 1997 for QSOs at $z < 0.3$; Yee & Green 1987 for $z \approx 0.6$). More recently, Grogin et al. (2005) find no evidence of enhancements in the local surroundings of AGNs at $z \sim 0.4$–1.3 in the GOODS fields.

To assess more formally if the AGNs possess an excess of companions relative to the overall galaxy population, we performed nearest neighbor statistics on the five ACS cluster fields. This test sometimes complements the two-point angular correlation function but is generally more sensitive to small-scale clustering (Osmer 1981; Scott & Tout 1989). Since the redshifts of the majority of the thousands of galaxies are unknown, we use the angular distance on the sky as a measure of the separation between the galaxies. From the positions in the SExtractor catalogs, we first calculate the separation of each galaxy to all other

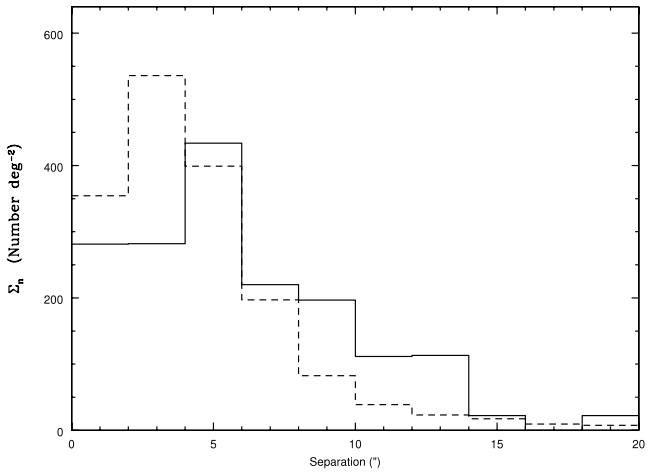

FIG. 13.—Composite histogram of the separations of the first nearest neighbors of the AGNs (*solid line*) and a random distribution of galaxies (*dashed line*) in the five cluster fields.

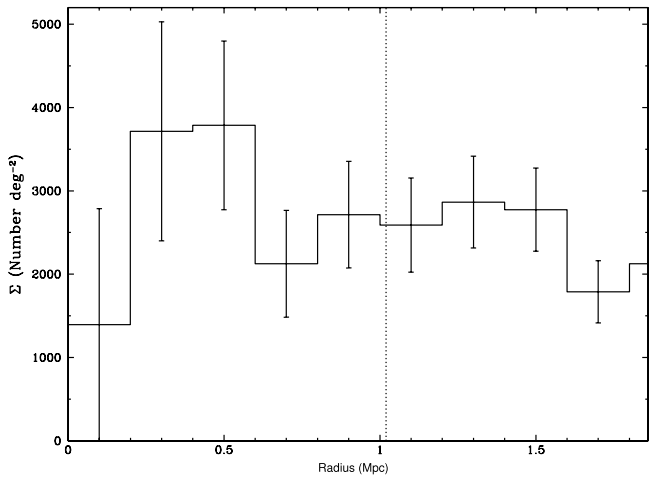

FIG. 14.—Composite surface density of the X-ray sources in the five clusters is plotted as a function of radius for annuli centered on the peak of the diffuse X-ray emission. The vertical dashed line marks the edge of the ACS field. Poissonian errors are assumed on the counts.

galaxies in the same field within an i_{775}-band magnitude range of -2 to $+1$ mags about the primary galaxy to limit background contamination. This typically results in a sample of $\approx$1200 galaxies. Frequency histograms of the first, second, third, etc., nearest-neighbor distances are then generated. The AGN-galaxy and galaxy-galaxy histograms are then extracted from these distributions. The latter serve as control samples and are assembled from 1000 realizations by randomly selecting galaxies that exclude the AGNs but match their magnitude distribution, irrespective of morphological type. Because of the small number of AGNs in the individual cluster fields, the frequency distributions of the five clusters are co-added to form a composite cluster.

The resulting surface density Σ_n of the first nearest neighbors, or pairs, is shown in Figure 13. The χ^2 test indicates that the disagreement between the two distributions is highly significant ($P \lesssim 1\%$). At separations of $5''$–$15''$, we find an excess of sources around the AGNs. The average excess is roughly 50% relative to the galaxy-galaxy population in the same fields. The apparent deficit of near neighbors among the AGN population at small separations ($\lesssim 3''$) is misleading because of the overlap of the light distributions of the galaxies in this regime. Indeed, the physical sizes of the galaxies, based on the distribution of their Kron radius as measured by SExtractor, are less than $3''$ and peak around $1.5''$. We therefore conclude that the surface density of sources around the X-ray–selected AGNs in the ACS GTO cluster fields is enhanced with respect to that of the overall galaxy population in the same fields.

3.6. *Radial Distribution*

The distribution of the AGNs in the clusters is also of importance since it can potentially offer clues to the triggering of the active phase, its lifetime, and the fueling mechanisms. Some studies indicate that AGNs and QSOs avoid the cluster cores. For example, the X-ray–selected AGNs in MS 1054 appear to strongly populate the radii 1–2 Mpc, suggesting that AGN activity is triggered by recent infall in the cluster outskirts (Johnson et al. 2003). On the other hand, the radio-loud AGNs are more likely found at smaller radii, indicating that the X-ray output might somehow get quenched during infall, at least below the X-ray detection thresholds (Best et al. 2002). This trend also appears to correlate with the decrease in star formation activity at small radii, including in the five ACS clusters of this study (van Dokkum et al. 2000; Homeier et al. 2005).

In Figure 14, the composite surface density Σ of the X-ray sources in the *Chandra* fields of the five clusters is plotted. The annuli are centered on the peak of the diffuse X-ray emission for RDCS J0910, MS 1054, and RDCS J1252, and for RX J0849, on the southern peak of RX J0849+4452. For RX J0152, the radial dependence is plotted with respect to its southern X-ray halo. Only sources above the flux limits of each field are considered. The radius of the outermost annulus is limited by the nearest edge of the *Chandra* fields. The vertical dashed line indicates the average extent of the ACS field of view for the five clusters. Although the errors are large, reflecting the small number of sources in each bin, there appears to be a trend for Σ to decrease as a function of radius. The surface density is highest at cluster radii of $\lesssim$1 Mpc and flat or possibly decreasing at larger distances. The ACS fields only cover the central regions ($\lesssim$1 Mpc), where Σ is typically highest but where the absolute number of X-ray sources is lowest.

There also appears to be a deficiency of X-ray sources in the cluster cores. In particular, for RX J0152, RX J0849, MS 1054, and RDCS J1252, no sources are found within a radius of $\sim$200 kpc of the peak of their X-ray halo. As pointed out by Demarco et al. (2005), the X-ray cluster members of RX J0152 are located close to the center but not exactly in the core. This is also true for the X-ray members of the other clusters. The six confirmed cluster members (see § 3.7) are located in a range of projected radii of 155–1400 kpc. Cluster membership will be necessary to fully constrain the true radial distribution of the X-ray sources in these clusters.

3.7. *The Cluster Members*

In Table 9, we list the X-ray sources with confirmed optical cluster counterparts based solely on their tabulated redshifts in Tables 4–8. We constrain the selection to sources with recessional velocities that are within $\pm$3500 km s^{-1} of the mean recessional velocity of their parent cluster. Are the host galaxies and environment of these AGN/QSO cluster members peculiar in any way? Although the numbers are small, there appears no strong preference for the AGN host morphologies: two are found in late-type hosts, three in early types, and one in an irregular galaxy. Half of the members appear to be part of interacting galaxy systems. ID 28 (RX J0152) and ID 51 (RDCS J0910) have projected galaxies of similar size and brightness within a

TABLE 9
Cluster Membership

Cluster	Cluster Members[a]
RX J0152−1357	23, 28
RX J0849+4452	...
RDCS J0910+5422	51, 65
MS 1054−0321	44
RDCS J1252−2927	131

[a] ID of the cluster members detected in the X-ray bandpasses (see Tables 4–8).

radius of $\lesssim 3''$ (25 kpc). Their host galaxies also show evidence of interaction such as tidal tails and asymmetric light distributions. ID 131 (RDCS J1252) is highly disturbed and possibly contains multiple nuclei. There are no obvious nearest neighbors in the immediate vicinity of the other three members and their host galaxies appear relatively unperturbed.

We can compare the sample of cluster members with the brighter ($i_{775} \lesssim 23$) optical counterparts of the other X-ray sources in the same fields. We find that ≈45% of the galaxies in this group possess a nearby companion or a small satellite galaxy in their halo, perhaps evidence of a "minor" merger, and a significantly large fraction (≈60%) of them also have disturbed or irregular host galaxies. Hence, we conclude that roughly half of the X-ray–selected AGNs, both cluster members and nonmembers, are part of a multiple galaxy system. The disturbed AGN hosts are more likely to be associated with a projected companion or satellite galaxy. We note that these estimates are based on visual inspection alone and no formal corrections are made for contamination.

4. CONCLUSIONS

Catalogs and optical images of the optical counterparts to the X-ray–selected AGNs and QSOs in the fields of five rich clusters ($z \approx 1$) imaged with ACS were presented. Three (RX J0152−1357, RDCS J0910+5422, and MS 1054−0321) of the five cluster fields show an overdensity of X-ray sources relative to the field sample of the CDF-S and CDF-N possibly due to the association of some sources with the cluster structures. The high spatial resolution and great depth of the ACS images permits accurate measurements of morphology and immediate environments of the counterparts. The asymmetry and concentration indices indicate that at magnitudes of $i_{775} \leq 25.5$, approximately half of the AGNs are located in early-type host galaxies, one-third in late types, and the remainder in irregulars. Roughly half of the early types possess a blue core. From visual inspection, unresolved nuclei appear more frequent in face-on late-type galaxies although selection effects may be important. The X-ray to nuclear optical flux ratio correlates with the inclination angle of the late types. The AGNs possess a ∼50% excess of companions at distances of $5''$–$15''$ compared to the general galaxy population in the same fields. The environment of the confirmed cluster members appears similar to that of the other AGNs in the ACS mosaics, but the small number of sources precludes any firm conclusion. The radial distribution of the X-ray sources is greatest at projected radii of ≲1 Mpc. Spectroscopic follow-ups are currently underway to secure the redshifts of the galaxies and to characterize their line and continuum properties.

P. Tozzi acknowledges support from the Johns Hopkins University during the completion of this work. ACS was developed under NASA contract NAS 5-32865, and this research has been supported by NASA grant NAG5-7697. The Space Telescope Science Institute is operated by AURA, Inc., under NASA contract NAS5-26555. We made use of the NASA/IPAC Extragalactic Database (NED), which is operated by the Jet Propulsion Laboratory, California Institute of Technology, under contract with NASA.

REFERENCES

Bahcall, J. N., Kirhakos, S., Saxe, D. H., & Schneider, D. P. 1997, ApJ, 479, 642
Bauer, F. E., Alexander, D. M., Brandt, W. N., Schneider, D. P., Treister, E., Hornschemeier, A. E., & Garmire, G. P. 2004, AJ, 128, 2048
Benítez, N. 2000, ApJ, 536, 571
Bertin, E., & Arnouts, S. 1996, A&AS, 117, 393
Best, P. N., van Dokkum, P. G., Franx, M., & Röttgering, H. J. A. 2002, MNRAS, 330, 17
Blakeslee, J. P., Anderson, K. R., Meurer, G. R., Benítez, N., & Magee, D. 2003a, in ASP Conf. Ser. 295, Astronomical Data Analysis Software and Systems XII, ed. H. E. Payne, R. I. Jedrzejewski, & R. N. Hook (San Francisco: ASP), 257
Blakeslee, J. P., et al. 2003b, ApJ, 596, L143
Cappi, M., et al. 2001, ApJ, 548, 624
Dahari, O. 1985, ApJS, 57, 643
Demarco, R., et al. 2005, A&A, 432, 381
Dressler, A., Smail, I., Poggianti, B. M., Butcher, H., Couch, W. J., Ellis, R. S., & Oemler, A., Jr. 1999, ApJS, 122, 51
Elmegreen, D. M., Elmegreen, B. G., & Ferguson, T. E. 2005, ApJ, 623, L71
Ford, H., et al. 2003, Proc. SPIE, 4854, 81
Friaça, A. C. S., & Terlevich, R. J. 2001, MNRAS, 325, 335
Fuentes-Williams, T., & Stocke, J. T. 1988, AJ, 96, 1235
Giacconi, R., et al. 2002, ApJS, 139, 369
Giavalisco, M., et al. 2004, ApJ, 600, L93
Gilli, R., et al. 2003, ApJ, 592, 721
Goto, T., et al. 2005, ApJ, 621, 188
Grogin, N. A., et al. 2003, ApJ, 595, 685
———. 2005, ApJ, 627, L97
Holden, B. P., et al. 2005, ApJ, 626, 809
Homeier, N. L., et al. 2005, ApJ, 621, 651
Jarvis, R. M., & MacAlpine, M. 1998, AJ, 116, 2624
Jeltema, T. E., Canizares, C. R., Bautz, M. W., Malm, M. R., Donahue, M., & Garmire, G. P. 2001, ApJ, 562, 124
Johnson, O., Best, P. N., & Almaini, O. 2003, MNRAS, 343, 924
Koekemoer, A. M., et al. 2004, ApJ, 600, L123
———. 2005, BAAS, 207, 63.55
Maoz, D., Barth, A. J., Sternberg, A., Filippenko, A. V., Ho, L. C., Macchetto, F. D., Rix, H.-W., & Schneider, D. P. 1996, AJ, 111, 2248
Martini, P., Kelson, D. D., Mulchaey, J. S., & Trager, S. C. 2002, ApJ, 576, L109
Maughan, B. J., Jones, L. R., Ebeling, H., Perlman, E., Rosati, P., Frye, C., & Mullis, C. R. 2003, ApJ, 587, 589
Mei, S., et al. 2006, ApJ, 639, 81
Menanteau, F., Abraham, R. G., & Ellis, R. S. 2001a, MNRAS, 322, 1
Menanteau, F., Ford, H. C. Motta, V., Benítez, N., Martel, A. R., Blakeslee, J. P., & Infante, L. 2006, AJ, 131, 208
Menanteau, F., Jimenez, R., & Matteucci, F. 2001b, ApJ, 562, L23
Menanteau, F., et al. 2004, ApJ, 612, 202
———. 2005a, ApJ, 620, 697
———. 2005b, BAAS, 207, 43.01
Molnar, S. M., Hughes, J. P., Donahue, M., & Marshall, J. 2002, ApJ, 573, L91
Osmer, P. S. 1981, ApJ, 247, 762
Pasquali, A., et al. 2006, ApJ, 636, 115
Postman, M., et al. 2005, ApJ, 623, 721
Rosati, P., Stanford, S. A., Eisenhardt, P. R., Elston, R., Spinrad, H., Stern, D., & Dey, A. 1999, AJ, 118, 76
Rosati, P., et al. 2002, ApJ, 566, 667
———. 2004, AJ, 127, 230
Sánchez, S. F., et al. 2004, ApJ, 614, 586
Schlegel, D. J., Finkbeiner, D. P., & Davis, M. 1998, ApJ, 500, 525
Scott, D., & Tout, C. A. 1989, MNRAS, 241, 109
Stanford, S. A., Holden, B., Rosati, P., Eisenhardt, P. R., Stern, D., Squires, G., & Spinrad, H. 2002, AJ, 123, 619
Stanford, S. A., Holden, B., Rosati, P., Tozzi, P., Borgani, S., Eisenhardt, P. R., & Spinrad, H. 2001, ApJ, 552, 504

Stern, D., Tozzi, P., Stanford, S. A., & Rosati, P. 2002, AJ, 123, 2223
Sun, M., & Murray, S. S. 2002, ApJ, 577, 139
Szokoly, G. P., et al. 2004, ApJS, 155, 271
Tozzi, P., et al. 2001, ApJ, 562, 42
Treu, T., Ellis, R. S., Liao, T. X., van Dokkum, P. G., Tozzi, P., Coil, A., Newman, J., Cooper, M. C., & Davis, M. 2005, ApJ, 633, 174
Urry, C. M., et al. 2005, BAAS, 207, 80.21
van Dokkum, P. G., Franx, M., Fabricant, D., Illingworth, G. D., & Kelson, D. D. 2000, ApJ, 541, 95
van Dokkum, P. G., Franx, M., Fabricant, D., Kelson, D. D., & Illingworth, G. D. 1999, ApJ, 520, L95
Virani, S. N., De Robertis, M. M., & VanDalfsen, M. L. 2000, AJ, 120, 1739
Yee, H. K. C., & Green, R. F. 1987, ApJ, 319, 28